MECHANISMS OF FATIGUE HARDENING IN COPPER SINGLE CRYSTALS

J. R. HANCOCK and J. C. GROSSKREUTZ
MIDWEST RESEARCH INSTITUTE

FOREWORD

This report was prepared by Midwest Research Institute, 425 Volker Boulevard, Kansas City, Missouri 64110, under USAF Contract No. AF 33(615)-3987. This contract was initiated under Project No. 7353, "Characterization of Solid Phase and Interphase Phenomena in Crystalline Substances," Task No. 735301, "Mechanical Metallurgy." Funds for this project are supplied to the Air Force Materials Laboratory by the Office of Aerospace Research. The work was monitored by the Air Force Materials Laboratory, Directorate of Laboratories, Air Force Systems Command, Wright-Patterson Air Force Base, Ohio, with Mr. D. M. Forney, MAMD, acting as Project Engineer.

This report covers work done during the period 1 April 1966 to 31 March 1967. The manuscript was released by the authors for publication in March 1967 as an AFML Technical Report.

Dr. J. C. Grosskreutz served as project leader during this research and Dr. J. R. Hancock and Mr. Douglas Day performed the majority of the experimental work.

This technical report has been reviewed and is approved.

W. J. TRAPP
Chief, Strength and Dynamics Branch
Metals and Ceramics Division
Air Force Materials Laboratory

ABSTRACT

An investigation of fatigue-hardening mechanisms in copper single crystals oriented for single slip was carried out for fully-reversed push-pull tests at a total resolved shear-strain amplitude of $\pm$ 0.008. Hysteresis loops and fatigue-hardening curves were recorded, and the dislocation structures were studied in annealed specimens and in cyclically hardened specimens after 4-1/2, 20, 100, and 660 cycles. Control specimens were irradiated with fast neutrons to prevent the loss and/or rearrangement of dislocations during electrothinning for transmission electron microscopy. No significant differences in dislocation density or morphology were detected between the irradiated and unirradiated crystals. The results indicated that dislocation structures in thin foils were representative of bulk material.

Fatigue hardening occurred by the accumulation and storage of dislocations into low-energy configurations characteristic of Stage I tensile hardening. The rapid-hardening stage was characterized by the rapid multiplication of dislocations and the build-up of cell-wall nuclei by the mutual trapping of primary edge dislocations on parallel slip planes. These bundles of primary edge dislocations (cell-wall nuclei) were aligned perpendicular to the primary Burgers vector and along the $\langle 110 \rangle$ critical and conjugate slip-plane traces. Edge bundles and mixed dislocations were preferentially aligned along these $\langle 110 \rangle$ directions as a result of an interaction with Frank partial-dislocation dipoles lying on the critical and conjugate slip planes. As cyclic straining proceeded, dislocations in the cell-wall nuclei became more densely packed and fragmented, and linked up to form a cell structure as saturation hardening developed. During saturation hardening, the applied strain could be accommodated by the traffic of dislocations across cells and/or cell-wall motion. Measurements of hysteresis loops indicated that 50 percent of the energy dissipated per cycle was available for point-defect production, which could yield a point-defect concentration of $\sim 10^{-6}$/cycle at 300°K.

CONTENTS

ILLUSTRATIONS

I.

INTRODUCTION

An understanding of fatigue-hardening mechanisms is essential to the further development of a crack propagation theory and to the elucidation of crack nucleation processes. In spite of the massive amount of experimental fatigue data available, relatively few experiments have been conducted under conditions most amenable to interpretation and analysis in terms of hardening mechanisms. This investigation is part of a larger program which was designed to meet the above needs by providing fatigue-hardening studies for a high-purity single-crystal metal under carefully selected conditions of temperature, shear-strain amplitude, strain rate, crystal orientation, environment, and mode of deformation. The study of the fatigue-hardening mechanisms in pure copper has the following objectives: (1) to determine the mechanisms of hardening and to formulate a quantitative theory of fatigue hardening for pure metals; (2) to determine the relationship between the saturation-hardening stress and the applied shear-strain amplitude; and (3) to assess the hardening that takes place at the tip of propagating fatigue cracks.

Two principal methods of study were employed in the investigation. Cyclic-strain hardening experiments were carried out and hysteresis loops were recorded as a function of the number of cycles. Transmission electron microscopy was then utilized to study the resulting dislocation arrangements at selected cumulative strains along the hardening curve. We have concentrated our observations of microstructures to the earliest stages of fatigue hardening in an effort to identify specific hardening mechanisms.

II.

EXPERIMENTAL PROCEDURES

A. Growth of Copper Single Crystals

Oriented single crystals seeded to a Schmid factor of 0.49 (single slip, approximately 5° from $[\bar{1}49]$ axis), were grown from ASARCO 99.999+ percent copper in a high-purity graphite mold. Three-eighths-inch diameter crystals were grown in 3-in. lengths at a rate of approximately 1 to 1-1/2 in. per hour using a Bridgeman technique. The graphite mold was designed so that six crystals could be grown at one time; after fusion with the seed, solidification proceeded through a 1/32-in. diameter orifice to eliminate sub-boundaries (Ref. 1). The elimination of sub-boundaries was subsequently verified by examination of thin foils in the electron microscope. From each of these crystals a 2-in. long fatigue specimen and a 1-in. seed were obtained. Back-reflection Laue patterns were taken of each crystal to verify that the orientation was correct. Table I lists the Schmid factors for the various slip systems for the $[\bar{1}49]$ axis.

TABLE I

SCHMID FACTORS FOR FAVORED SLIP SYSTEMS
FOR $[\bar{1}49]$ SPECIMEN AXIS

Slip System	Schmid Factors	
	Calculated	Measured
(111) $[\bar{1}01]$; Primary system	0.50	0.49
$(1\bar{1}1)$ $[\bar{1}01]$; Cross-slip system	0.17	-
$(\bar{1}11)$ $[101]$; Critical-slip system	0.47	-
$(\bar{1}\bar{1}1)$ $[011]$; Conjugate-slip system	0.33	-

B. Preparation of Fatigue Specimens

Fatigue specimens were prepared (see Figure 1) by machining the gauge length on a Servomet spark-cutting machine to approximately 0.24 cm. diameter by 0.825 cm. long. When subsequently sectioned for transmission electron microscopy, specimens of this diameter fit directly into the Hitachi HU-11, electron-microscope specimen holder. In addition, five grooves approximately 0.075 cm. wide by 0.012 cm. deep were machined into the gripping ends of the specimens. These grooves were found necessary to ensure a hard

loading column and provided a purely mechanical means of gripping the specimens when mounted in Wood's metal (described under Section II-D). The gauge-length dimenions were governed principally by the maximum tolerable load in the Wood's metal and the length to diameter ratio, L/D, required to eliminate buckling. An L/D ratio of $\approx$ 4 has been employed successfully.

Each crystal was then annealed under vacuum (10^{-5} to 10^{-6} torr) in a high-purity graphite boat for 4 hr. at 950°C and furnace cooled. Prior to use the crystals were cleaned in dilute nitric acid, the gripping ends tinned with soft solder to promote wetting by the Wood's metal during mounting, and the gauge length electropolished at room temperature in standard Disapol electrolyte D2 at approximately 10 volts. The diameters and gauge lengths were measured optically to approximately $\pm$ 0.003 cm.

C. Cyclic-Strain Fixture

A loading fixture was constructed of 304 stainless steel and attached to the bottom of the moveable cross head on an Instron testing machine. The fixture is designed to allow all testing to be carried out in a helium environment and allows the desired test temperature to be maintained by immersing the fixture and specimen in an appropriate liquid bath. The enclosed test chamber allows us to eliminate possible extraneous surface effects of the different liquids used for temperature control. Figure 2 is a line drawing and Figure 3 a photograph of the loading fixture (including an LVDT extensometer) mounted on the Instron testing machine. The fatigue specimen is mounted in Wood's metal for the room temperature (300°K) tests or in tin babbitt alloy 2 (ASTM-B23-49; 89Sn, 7.5Sb, 3.5Cu; melting range: 241 - 354°C) (Ref. 2), for the test carried out at 425°K. This mounting technique allows careful alignment and precludes accidental straining of the specimen during mounting. The helium-filled specimen chamber is enclosed with a tightly fitting neoprene or silicon-rubber bellows which fits over the ends of the loading column.

Because of the difficulty in achieving perfect axial alignment of the long (11-3/4 in.) loading fixture, the bottom of the fixture executes a small transverse motion during cycling which produces an additional shear strain in the specimen. Assuming that the specimen accommodates the entire transverse motion, an additional shear strain equal to $\approx$ 12 percent of the total resolved shear strain is produced.

An extensometer designed for use over a wide temperature range (Ref. 3) was constructed of 304 stainless steel and Teflon (Figures 2 and 3); split-gripping plates are attached to the loading column above and below the specimen and eliminate the effects of linkages in the loading column. The differential displacement of the core and coil of the LVD transformers

was used to control the strain amplitude through the calibrated limit switches on a Datronic 300 CL/62 instrument. Addition of the electrical outputs of the dual LVD transformers eliminated bending effects and doubled the sensitivity of the extensometer.

D. Cyclic-Strain Tests

Fatigue specimens were mounted in the upper grip in the following manner. The specimen was held in a Teflon split-gripping ring which screwed into the objective lens housing on a tool-maker's microscope and the upper gripping head of the loading fixture was centered beneath the specimen. Vertical alignment was achieved optically using a cathetometer. Wood's metal was melted in the gripping head with a resistance-soldering unit and the specimen was then lowered into the Wood's metal using the vertical travel of the microscope. The Wood's metal was allowed to freeze (melting point = 75°C) and the assembly was next attached to the loading column on the Instron testing machine. Wood's metal was then melted in the lower gripping head and the specimen was lowered into the melt by means of the cross-head travel. After solidification the neoprene bellows was positioned in place and the chamber was flushed with helium. The helium environment was maintained throughout the test. The load on the specimen was manually maintained at zero until testing began. This was necessary because of the volume changes which occur in Wood's metal for 2 to 3 hr. after solidification. After mounting the specimens in the higher-melting tin babbit for the tests conducted at 425°K, the gauge lengths were re-electropolished *in situ* to remove oxidation products.

Cyclic-strain-hardening experiments were carried out with polycrystalline specimens at room temperature for a variety of strain amplitudes and with single crystals at a total shear strain amplitude of $\pm$ 0.008 both at 300°K (room temperature) and 425°K. The load was recorded on the Instron strip chart and the signals from the load cell and LVD transformers were fed into an X-Y recorder to plot the change in size and shape of hysteresis loops as cycling proceeded. A tensile strain was always applied for the first quarter cycle. Cyclic-strain-hardening experiments on single crystals were terminated at N = 4-1/2, 20, 100, 660 cycles for subsequent transmission electron microscopy. Upon termination of the test, specimens were carefully cut out of the grips with a jeweler's saw.

E. Specimen Preparation for Transmission Electron Microscopy

Figure 4 shows the orientation of the single crystals employed and the orientation and geometry of discs prepared for transmission electron microscopy (TEM). Discs were sectioned so that the primary slip plane (111) was

approximately parallel to the foil surface. Figure 5 illustrates the procedures used in preparing discs for TEM. The gauge lengths of the single-crystal fatigue specimens were oriented for sectioning by means of primary slip traces under an optical microscope and specimens were then cemented to a metal support (Figure 5B). Discs 0.030-in. thick were then sectioned along the primary slip plane on a Servomet spark-cutting machine. The discs were thus elliptical with their major axis parallel to the primary slip direction $[\bar{1}01]$ (Figure 4). The minor axis (0.22 cm.) of the elipse was small enough in relation to the electron-microscope specimen holder so that the edge of the disc could be viewed in the microscope and used to establish the direction of the primary slip vector on micrographs. The discs were subsequently indented with a 0.054-in. diameter steel tool on the spark-cutting machine to a depth of approximately 0.008 in. They were then spring-loaded in a small strain-free mounting of platinum wire. The wire was gripped with stainless-steel tweezers and all nonessential areas were masked with a nonconducting lacquer (Microstop). An area on each side of the disc, slightly larger than the 0.054-in. diameter indentation, was electrothinned, removing approximately 0.011 in. from each side.

The polishing conditions found to be most satisfactory were as follows: a 2:1 mixture of methanol:nitric acid at -25°C, 1.5 volts, 0.11 amps/cm^2. (For initial thinning, slightly higher values of current and temperature can be used.) The specimens were continuously observed and the circuit was broken when light from a source on the opposite side of the disc could be seen. The specimens were subsequently washed in distilled water and in methanol at room temperature. The Microstop was dissolved in acetone and the specimen was rewashed and dried by placing it on filter paper.

Discs of the thickness employed (0.030 in.) were relatively rugged TEM specimens and reduced the possibility of accidental damage during handling. As a further precaution the discs were held in place in the electron-microscope specimen holder with a small (0.008-in. diameter wire) bronze spring instead of the solid insert normally used. This arrangement was quite successful in preventing specimen damage during handling.

F. Reliability of Thin-Foil Observations

In order to determine the extent of dislocation loss and/or rearrangement during electrothinning for transmission electron microscopy, annealed single crystals and crystals fatigued to 20, 100, and 660 cycles were irradiated with fast neutrons (> 0.4 Mev to 1.37×10^{18} nvt) to pin the dislocations and preserve the bulk dislocation structure.

III.

EXPERIMENTAL RESULTS

A. Cyclic-Strain Hardening

Details of cyclic-strain-hardening conditions and results are tabulated in Table II. Hardening curves are shown for polycrystalline copper in Figure 6 and for copper single crystals in Figure 7. All single-crystal tests were carried out for a total resolved shear-strain amplitude, γ_t, of $\pm$ 0.008. The equivalent resolved shear stress plotted in Figure 6 is 0.435 times the normal axial stress. (An equivalent resolved shear strain for polycrystalline specimens was simulated by taking the axial normal strain as 0.435 times the resolved shear-strain amplitude used for single crystals (Ref. 4).)

The hysteresis loops for a single crystal for the first 25 cycles are shown in Figure 8. The curves in Figure 7 represent the results from a number of specimens (Table II) and the hardening curves for undamaged specimens are virtually identical. The results shown in Figures 6 and 7 are in general accord with published data for copper. That is, the initial hardening rate (rapid hardening) is higher for polycrystalline specimens and for higher temperatures, and the saturation stress is higher for larger strain amplitudes and for lower temperatures (see, e.g., Refs. 5, 6 and 7). The saturation stress, τ, for $\gamma_t = \pm$ 0.008 is 416 kg/cm^{-2} for polycrystalline specimens at room temperature, 335 kg/cm^{-2} for the single crystals at room temperature and 238 kg/cm^{-2} at 425°K. Specimens which were inadvertently bent during mounting always hardened more rapidly, though the saturation stress was unaffected.

Areas of hysteresis loops were measured with a planimeter for specimens M8 (300°K) and for M12 and M15 (both 425°K). These measurements were converted to energy dissipated/cm^3/cycle and plotted versus cumulative total shear strain in Figure 9. The trend of these curves is the same as for those in Figure 7. If it is assumed that this plastic-strain energy is converted to thermal energy and dissipated entirely as heat, the resultant temperature rise is quite insignificant. For specimens M8 (300°K) and M13 (425°K) at saturation, the energy, E, dissipated is 5.75 x 10^6 and 3.94 x 10^6 ergs/cm^3/cycle, respectively (0.1370 and 0.0943 calories/cm^3/cycle, respectively). The maximum instantaneous (taken here as one cycle which is about 7 - 8 sec.) temperature rise is $\Delta T = \frac{E}{\rho C}$ where ρ is the density of copper and C the specific heat. Thus $\Delta T \cong 0.164$°C/cycle for M8 at 300°K and $\Delta T = 0.112$°C/cycle for M12 at 425°K. At a cyclic frequency of 8 cpm it would require approximately 1 min. to achieve a 1°C rise in temperature assuming no heat loss to surroundings. In view of the good thermal contact with the specimen it is doubtful that any significant bulk-temperature rise occurred during these cyclic tests.

TABLE II

FATIGUE-HARDENING DATA FOR HIGH-PURITY COPPER

Specimen[a]	Total N	γ_t	Temperature (°K)	τ_{Sat} (kg/cm^2)	Remarks	TEM
P5	410	±0.008	300	416	Bent prior to test	x
P6	330	±0.0105 (γ_p)[d]	300	535	-	x
P7	370	±0.0105	300	470	-	-
P8	330	±0.0167	300	546	-	-
M1	662	±0.008	300	340	Bent prior to test	x
M3	19	±0.008	300	-	Bent prior to test	-
M4[b]	100	±0.008	300	$(314)_{N=100}$	Irradiated	x
M6[b]	20	±0.008	300	-	Irradiated	x
M7	662	±0.008	300	310	Specimen buckled at ≈ N = 35	-
M8[b]	662	±0.008	300	333	Irradiated	x
M10[b]	0	-	-	-	Control specimen for irradiation experiments	x
M22	20	±0.008	300	-	-	x
M34	100	±0.008	300	$(323)_{N=100}$	-	x
M35	660	±0.008	300	314	Buckled slightly	-
M36	4.5	±0.008	300	-	-	x
M38	4.5	±0.008	300	-	-	-
M40	179	±0.008	300	318	-	-
	218	±0.0025	300	278		
M11	150	±0.008	425	238	Bent prior to test	-
M12[b]	225	±0.008	425	238	Irradiated	-
M13	225	±0.008	425	238	Bent prior to test	-

TABLE II (Concluded)

Specimen[a]	Total N	γ_t	Temperature (°K)	τ_{Sat} (kg/cm^2)	Remarks	TEM
M14[b]	10	$\pm$0.008	425	-	Irradiated	-
M15[b]	45	$\pm$0.008	425	-	Irradiated	-
MS17[b,c]	0	-	-	-	Control specimen for irradiation experiments	-

a/ Omission of certain specimen numbers indicates crystals which were subsequently discarded after having been damaged or after X-ray examination revealed that the orientation was not [$\bar{1}$49].

b/ Specimens which were irradiated in The Phoenix Memorial Laboratory Reactor Facility, University of Michigan, Ann Arbor.

c/ Notation "MS" denotes that a "seed" crystal (1 in. in length) was used for the irradiation specimen as opposed to using a 2-in. crystal, M17, in the interest of conserving specimens.

d/ The plastic strain amplitude was held constant for specimen P6; in all other tests the total strain amplitude was held constant.

P Polycrystalline specimens.

M Monocrystalline specimens (Schmid Factor = 0.49).

Figure 10 shows the results obtained for a single crystal which was cyclically hardened ($\gamma_t = \pm 0.008$) into the saturation region and then cyclically softened by changing to a lower strain amplitude ($\gamma_t = \pm 0.0025$). The strain amplitude was reduced manually by adjusting the settings of the limit switches on the Daytronic instrument over a duration of 7 cycles. An abrupt reduction in strain amplitude results in an abrupt reduction in stress amplitude. Thus, the dotted line shown in Figure 10 does not represent a real softening rate. Following this reduction in strain amplitude, the maximum stress amplitude begins to decrease (softening begins) from an initial value which lies on the hysteresis loop established at the higher strain level. The rate of softening decreases with continued cycling and a new saturation stress level is established.

B. Transmission Electron Microscopy

A limited amount of transmission electron microscopy (TEM) was carried out on the polycrystalline specimens during the development of thinning procedures. All of the remaining TEM was carried out on single crystals, for N = 0, and for crystals cyclically hardened at $\gamma_t = \pm 0.008$, 300°K to N = 4-1/2, 20, 100, and 660 cycles. All crystals were sectioned parallel to the primary slip plane.

Representative micrographs obtained from polycrystalline specimens P5 and P6 are shown in Figures 11 and 12, respectively. These specimens were cycled well into saturation and the cell structure was well developed with very high dislocation densities within the cell walls and with relatively few dislocations in the centers of the cells. The cell size decreased with higher strain amplitude and cell walls tended to lie along close-packed $< 110 >$ directions. Many elongated dipoles can be seen in Figure 11.

Figures 13A and 13B show the microstructure in an annealed and irradiated copper single crystal. The small dark spots are dislocation loops produced by the precipitation of irradiation-induced point defects. In Figure 13B a dislocation in screw orientation has produced a long (greater than 3 microns) edge dipole as a result of a drag exerted on the screw segment by a super jog. The dipole appears to be in the process of pinching off at the end; this could be a result of climb induced by the neutron irradiation. Other evidence of climb was observed in fatigued and irradiated specimens; that is, dislocations, and particularly dipoles, appeared to contain a greater number of large jogs in the irradiated crystals. The dislocation densities (exclusive of the irradiation damage) in the annealed copper single crystals were 10^7 to 10^8 cm^{-2}.

Figures 14 through 17 show representative microstructures in cyclically-hardened copper single crystals at progressively increasing numbers of

cycles. Figures 14A and 14B show the dislocation arrangements after 4-1/2 cycles (rapid-hardening stage). Dominant features of these typical micrographs are (a) the nonuniform distribution of dislocations, (b) the presence of prismatic closed-loop dipoles, elongated in the $[1\bar{2}1]$ direction, (c) the bundles of dislocations in edge orientation, (d) the presence of Frank partial dislocations (in faint contrast) (Ref. 8) lying along the traces of the critical and conjugate slip planes (see also Figure 21), and (e) the tendency for cell walls to build up, not only in the $[1\bar{2}1]$ direction, but also along the critical and conjugate slip-plane traces in association with the Frank partials (see Figure 21). Also shown in Figure 14A are examples of the formation of elongated dipoles behind gliding screw dislocations. Burgers vector determinations have not been made for these dislocations; however, the majority probably possess the primary $1/2[\bar{1}01]$ Burgers vector.

Figures 15A and 15B show the dislocation arrangements after 20 cycles (rapid-hardening stage). The same features observed after 4-1/2 cycles are present. Major changes are the increase in dislocation density and dipole density, the continued build-up and linkage of cell-wall nuclei into a cell structure, and the increased density and the fragmentation of dislocations within cell walls. The dislocations within the cell wall become very densely packed and are no longer resolvable as individual dislocations.

Figures 16A and 16B are representative micrographs showing the dislocation arrangements after 100 cycles (almost in saturation-hardening stage). The operating reflection for the upper right hand corner of Figure 16A is $g = [\bar{1}1\bar{1}]$ which renders dislocations possessing the primary $1/2[\bar{1}01]$ Burgers vector invisible. This demonstrates that a great many dislocations with other than the primary Burgers vectors are present and that plastic flow has probably been active on other slip planes during the first 100 cycles. The cell walls that are in contrast exhibit a tendency to align along traces of the critical and conjugate slip planes as noted earlier.

Figures 17A and 17B conclude the series of micrographs showing microstructures as a function of the number of cycles and shows representative structures after 660 cycles. The major changes that occurred between 100 and 660 cycles are the continued build-up and fragmentation of densely-packed dislocations into sharply-defined cell walls, and an increased misorientation across cell walls.

Table III summarizes the quantitative results of the TEM studies. As cycling proceeded, the dislocation density increased from 10^7 to 10^8 in the annealed crystals to approximately 6×10^9 cm^{-2} at 20 cycles. It is not feasible to measure dislocation densities for structures exhibiting a pronounced cell structure, as for N = 100 and 660, because individual dislocations in the cell walls cannot be resolved, and the statistical variation of dislocations within cells is large.

TABLE III

SINGLE-CRYSTAL SPECIMENS, HISTORY, AND DISLOCATION DENSITIES

Specimen	N	τSat (kg/cm^2)	Dislocation Density, cm^{-2}	Primary Dipole Density, cm^{-3}
MS35	0	-	10^7 - 10^8	-
M10 (Irradiated)	0	-	10^7 - 10^8	-
M36	4-1/2	-	2×10^9	3×10^{12}
M22	20	-	$5\text{-}7 \times 10^9$	9×10^{12}
M6 (Irradiated)	20	-	-	-
M34	100	(323)	-	-
M4 (Irradiated)	100	(314)	-	-
M35	660	314	-	-
M8 (Irradiated)	660	333	-	5×10^{13}

C. Reliability of Thin-Foil Observations

We do not yet have sufficient data for the irradiated specimens to draw a firm conclusion regarding dislocation losses and/or rearrangements during electrothinning for TEM. It appears generally true, however, that a greater number of isolated dislocations can be found in the irradiated specimens than in unirradiated specimens, indicating that the neutron irradiation was effective in pinning the dislocations and preventing their loss during thinning. The effect, however, appears to be relatively small, confined to the loss of relatively free dislocations within the cells, and no major dislocation rearrangements were detectable. Figures 17 and 18 show an example of the type of dislocations that are prevented from being lost during thinning. Long isolated dislocations, appearing joggy as a result of the irradiation-induced climb, are effectively pinned; these isolated dislocations account for less than an estimated five percent of the total dislocation density, and is within the experimental error of determining dislocation densities ($\approx \pm 20$ percent). These isolated dislocations are seen with less frequency in unirradiated specimens; nevertheless, they can be found in some areas (Figure 19).

Figure 20 shows the results of measurements of the foil thickness and dislocation densities in crystal M22. The thickness was calculated from measurements on a single twin trace for a known orientation, and consequently, yield unusually consistent dislocation densities over a broad range of thickness. The dislocation density was observed to be constant over the entire thickness range down to approximately 700 to 800 Å, where accurate thickness measurements were not available. In the 700 to 800 Å range the dislocation density appeared to decrease rapidly.

IV.

DISCUSSION OF RESULTS

A. Reliability of Thin-Foil Observations

The results shown in Figures 18 - 20 are strong evidence that the loss and/or rearrangement of dislocations during electrothinning is not serious where the thickness of the foil is greater than about 1000 Å. Dislocation densities in some regions of neutron-irradiated specimens are estimated to be at most 5 percent higher than in unirradiated specimens. If large numbers of dislocations are lost during thinning then they are lost almost as easily from the neutron-irradiated specimens as from unirradiated specimens. We believe this to be highly unlikely.

It has been suggested by some workers that the absence of screw dislocations in thin foils is due to their loss during electrothinning. It has been our observation that isolated screw dislocations are seen with more frequency in the early stages of hardening (4-1/2 and 20 cycles, Figures 15 and 21C) than after saturation hardening has occurred. This observation indicates that screw dislocations may be preferentially eliminated during cyclic straining, or aligned into a mixed orientation rather than lost during thinning. Similar conclusions have been drawn in the case of unidirectional deformation (Refs. 9 - 11).

We may conclude, therefore, that the dislocation arrangements which we observe are representative of the bulk material.

B. Dislocation Arrangements During Hardening

It has become accepted practice in discussions of fatigue hardening and fracture to classify the magnitude of the stress or strain amplitude as "high" or "low". Although the dividing line between these two arbitrary regions is somewhat vague and dependent on the material, the experiment to be discussed here should be classified as intermediate to high shear-strain amplitude ($\pm$ 0.008). This region of applicability should be kept in mind when comparing the results to those of other workers in the field.

The observations made during the rapid-hardening stage yield the clearest understanding of the fatigue-hardening process in copper. Figure 21 shows additional examples of the dislocation morphology after 4-1/2 cycles at 300°K. The dominant features are the bundles of primary edge dislocations and the alignment of these bundles along critical and conjugate slip-plane traces. Also present are isolated prismatic dipoles, some of which

can be seen in the process of formation (Figures 21C), and Frank partial dipoles which may be seen in Figure 21C. All of these features have also been observed after unidirectional deformation of copper single crystals into Stage I (Refs. 8 - 11). Our strain amplitude, 0.008, is well within Stage I for copper (Ref. 12), hence, the first few reversals of this strain simply serve to accentuate and accumulate the dislocation morphology characteristic of Stage I.

The dislocation bundles contain edge dislocations (on parallel slip planes) which have interacted over a portion of their length with dislocations of opposite sign to form dipoles (not necessarily terminated), or of the same sign to form tilt walls. The dipoles are probably formed by a mutual-trapping mechanism. In addition, prismatic closed-loop dipoles (formed by jogged screw dislocations) can be swept into these dislocation bundles by newly arriving dislocations (Refs. 13 and 14). Even at this early stage of hardening, the dislocation bundles can be viewed as the nuclei of future cell walls, Figure 22. Bundles of dislocations in predominately edge orientation have also been observed after Stage I tensile hardening of aluminum (Ref. 15), and cobalt-nickel (Ref. 16).

It is clear from the micrographs (Figures 21B and 21C) that a strong interaction exists between the Frank partial dislocations and the primary dislocations, resulting in a preferential alignment of the dislocation bundles along $\langle 110 \rangle$ directions. The details of the origin of the Frank partials is not clear. Hirsch (Ref. 8) indicates that a jog of a mixed dislocation could dissociate under an applied stress into Shockley and Frank partial dislocations (dipoles). As the primary dislocation advances, the glissile Shockley partial advances with it and extends the fault. Once a Frank partial has formed, the trapping of primary dislocations begins and this in turn may promote the formation of additional Frank partials. Figures 21B and 21C show evidences of such trapping at (e).

Thus for the strain amplitude employed, the rapid-hardening stage in copper is dominated by the rapid multiplication of dislocations and their clustering into edge bundles. These bundles lie along $\langle 110 \rangle$ directions in association with Frank partials, and along the $[1\bar{2}1]$ direction as a natural consequence of their edge orientation.

As cycling progresses through 20, 100, and 660 cycles the dislocation density continues to increase and the dislocation bundles become more sharply defined and form a cell structure on the primary glide planes. Comparison of the micrographs taken at 660 cycles with those at 100 cycles reveals that considerable cell-wall activity has occurred during the prolonged cycling. That is, dislocations in the cell walls have been chopped up into shorter segments, presumably as a result of climb and dislocation interaction. It is also quite clear (Figure 16A) that extensive dislocation multiplication and glide has occurred on secondary slip systems.

Our observations have been restricted to sections parallel to the primary glide plane and do not establish whether the cell structure is really a completely enclosed three-dimensional structure. We have never observed, for example, the low-angle twist boundaries which Laufer and Roberts (Ref. 17) observed after prolonged fatigue cycling. The possibility exists, therefore, that the cells which form in 660 cycles remain essentially two-dimensional in character for single-slip crystals, i.e., they are not enclosed parallel to the primary slip plane.

At lower strain amplitudes Segall, et al., (Ref. 18) have observed that cell structures do not form in copper, even after prolonged cycling. We believe that the patches of dislocation loops and dipoles which they report are entirely analogous to the bundles of nearly edge dislocations which we observe in the early stages of hardening at the higher strain amplitude. It is reasonable to believe that the effect of the higher amplitude is simply to promote the organization of the dislocation bundles (which are formed at all amplitudes) into a regular cell structure.

C. Saturation Hardening

The saturation stage of fatigue hardening is characterized by a hardening rate which approaches zero. Three mechanisms for accommodating the applied strain in the saturation stage are: (1) the flip-flop motion of prismatic dipoles (Ref. 6); (2) the traffic of dislocations across the cells or between dislocation bundles, and (3) the two and fro motion of dislocations within cell walls (or bundles). The first mechanism could be logically considered a special case of (3); however, we list it separately because of the special treatment it has received by Feltner (Ref. 6).

Evidence of dislocation traffic across cells is gained from micrographs such as Figures 17 - 19 which shows dislocations lying across the interior of cells. Direct evidence for the motion of cell walls and/or the dislocations within them is, of course, not available from micrographs of the residual dislocation arrangements. Nevertheless, some insight into the plausibility of these two possible mechanisms can be gained from simple calculations of the number of dislocations required and the displacements involved in each case. A further check on the validity of these mechanisms is afforded by calculation of the energy dissipated per cycle which can be compared with the experimentally observed energy dissipation (area of hysterises loop) during saturation.

Consider first the number of dislocations moving across cells which would be required to accommodate the applied strain. The basic equation is

$$\gamma = Nbd$$

where N is the dislocation density, b the Burgers vector, and d the average glide distance of a dislocation. If we take d to be the average cell dimension ($1.2\,\mu$) and substitute for N the quantity m/d^2, where m is the number of dislocations per cell which move on any given cycle, then we calculate $m = 38$ for $\gamma = \pm 0.008$, in essential agreement with Feltner and Laird (Ref. 19), who worked at $\gamma = \pm 0.05$.

We can also derive a value for m by considering the total energy required to push these dislocations across a cell for any given cycle. The work required to move one dislocation across a cell of dimension d is

$$W = b\tau d^2$$

where τ is the resolved shear stress on the primary slip plane. The work required to move m dislocations is simply mW. If we take the number of cells per unit volume as $1/d^3$, the energy dissipation per unit volume is:

$$E = \frac{mb\tau}{d}$$

If we equate this to the measured energy dissipation during saturation, 5.75×10^6 ergs/cm^3, we obtain a value for $m = 85$ dislocations. The fact that this value exceeds that required to accommodate the applied strain indicates that ~ 50 percent of the energy is dissipated by other processes, e.g., point-defect production.

One can also calculate the amount of cell-wall motion necessary to accommodate the applied strain (assuming that mechanism (3) applies). If the cell wall contains equal numbers of dislocations of opposite signs, then it will simply expand and contract under the alternating strain. If there is an excess of dislocations of one sign, then localized regions of the cell wall will actually move to and fro as an entity. In either case one can estimate the average distance which a dislocation must move in order to accommodate the saturation strain. If $\bar{x}$ is the average displacement of a dislocation in the wall, then

$$\bar{x} = \gamma/Nb$$

where N is an average dislocation density which is obtained by averaging the number of dislocations in the cell walls over the total crystal volume. This calculation ignores the question of cell-wall orientation and the fact that the resolved shear strain will be different across different cell walls. We have not measured the density of dislocations in the cell walls because of the difficulty of resolving individual dislocations; however, we may estimate this density as $\sim 10^{13}/cm^2$. If the cell-wall width is ~ 0.1 of the cell dimension, then $N = 2 \times 10^{12}/cm^2$, and $\bar{x} = 16$ Å. This value probably underestimates the actual motion which is necessary to accommodate the strain because of orientation effects and the fact that cell walls will be pinned at their intersection with other walls. Even if $\bar{x}$ were ten times the calculated value, the average motion of cell walls would be very small compared to the cell dimension.

The energy necessary to accomplish this cell-wall motion again accounts for only ~ 50 percent of the total measured energy dissipated per cycle, so that other dissipative mechanisms such as point-defect production must also be invoked. If half of the energy dissipated were equated to vacancy and interstitial production and diffusion, a point-defect concentration of approximately 10^{-6} per cycle would be generated. Weissmann, et al., (Ref. 20) have recently attributed the mobility of cell walls during cyclic straining to a climb mechanism which would involve vacancies.

On the basis of our experiments and the above calculations we are not able to make an unambiguous choice between mechanisms (2) and (3) to account for saturation hardening. Slip-band formation at free surfaces and our observation of dislocations within cells indicates that some traffic of dislocations across cells takes place. However, the fact that dislocations within cells do not occur frequently (even in neutron-irradiated material) favors the third mechanism of cell-wall motion. Thus a minority of strain can be accounted for by to and fro traffic and the majority by cell-wall motion. Approximately half of the total energy dissipated would remain for point-defect production and climb. Feltner and Laird (Ref. 19) have also considered both of these mechanisms recently to explain their results on polycrystalline Cu and Cu-7.5 percent Al.

V.

CONCLUSIONS: FATIGUE-HARDENING MODEL

Based on the observations reported here, fatigue hardening of copper single crystals at intermediate to high-strain amplitudes can be summarized in the following manner:

The initial rapid-hardening stage is characterized by the rapid multiplication of dislocations and their storage into low energy configurations. These configurations consists initially of bundles of primary edge dislocations aligned along the $[1\bar{2}1]$ direction or along the $\langle 110 \rangle$ directions corresponding to the traces of the critical and conjugate slip planes. The mechanism by which these dislocation bundles are formed is by mutual trapping of edge dislocations gliding on parallel slip planes. These bundles are thought to be immobilized by their interaction with Frank partial dislocations which form on the critical and conjugate slip planes. Concomitant with this stage of rapid hardening is the formation of prismatic closed-loop dipoles at large jogs on screw dislocations. These dipoles and other point-defect debris are swept into the primary edge bundles by newly arriving dislocations.

The transition from rapid hardening to saturation hardening occurs by the formation of a cell structure whose walls consist of the aforementioned dislocation bundles. The hardening which occurs is due primarily to dislocation multiplication and the limitation of dislocation mean-free-path by the cell structure. The final value of the saturation stress is inversely proportional to the mean cell dimension as originally suggested by Grosskreutz (Ref. 21) and confirmed by Pratt (Ref. 22). The effect of increasing temperature is to decrease the value of the saturation stress. This observation is consistent with the model, for Pratt (Ref. 23) has observed the cell size formed at a given applied strain amplitude to increase with temperature.

REFERENCES

1. Dyer, Lawrence D. JAP, 36, 301 (1965).

2. Metals Handbook, 1, Properties and Selection of Materials, ASM, p. 1145 (1961).

3. Feltner, C. E., "An Extensometer for Use at Low Temperatures," Ford Motor Company, Scientific Laboratory Publication Preprint, 12 June 1964.

4. Kemsley, D. S., and M. S. Patterson, Acta Met., 8, 453 (1960).

5. Avery, D. H., and W. A. Backofen, Fracture of Solids, AIME Conference, 20, Interscience Publishers, 339 (1963).

6. Feltner, C. E., Phil. Mag., 12, 1229 (1965).

7. Wadsworth, N. J., Acta Met., 11, 663 (1963).

8. Hirsch, P. B., "The Relation Between the Structure and Mechanical Properties of Metals," HMSO, 40 (1963).

9. Basiński, F. S., Dislocations in Solids, Discussions of the Faraday Society, No. 38, 93 (1964).

10. Essman, U., Phys. Stat. Sol., 12, 707 (1965).

11. Steeds, J. W., and P. M. Hazzledine, Dislocations in Solids, Discussions of the Faraday Society, No. 38, 103 (1964).

12. Mitchell, T. E., and P. R. Thornton, Phil. Mag., 8, 1127 (1963).

13. Sharp, J. V., and M. J. Makin, Phil. Mag., 10, 1011 (1964).

14. Chen, H. S., J. J. Gilman, and A. K. Head, JAP, 35, 2502 (1964).

15. Wilsdorf, H. G. F., and J. Schmitz, JAP, 33, 1750 (1962).

16. Mader, S., A. Seeger, and H. M. Thieringer, JAP, 34, 3376 (1963).

17. Laufer, E. E., and W. N. Roberts, Phil. Mag., 14, 65 (1966).

18. Segall, R. L., P. G. Partridge, and P. B. Hirsch, Phil. Mag., 6, 1493 (1961).

REFERENCES (Concluded)

19. Feltner, C. E., and C. Laird, "Cyclic Stress Strain Response of FCC Metals and Alloys; II. Dislocation Structures and Mechanisms," Ford Motor Company, Scientific Laboratory Publication Preprint, 17 November 1966.

20. Weissmann, S., A. Shrier, and V. Greenhut, Trans. ASM, 59, 709 (1966).

21. Grosskreutz, J. C., "Fatigue - An Interdisciplinary Approach," Syracuse U. Press, 27 (1964).

22. Pratt, J. E., J. of Materials, 1, 77 (1966).

23. Pratt, J. E., Acta Met., 15, 319 (1967).

a. Single Crystal

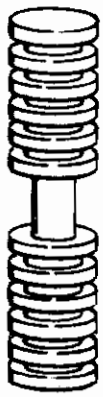

b. Grooves and gage length machined on spark-cutting machine using a lathe attachment

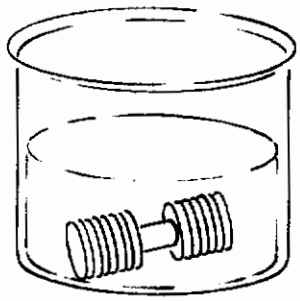

c. Remove damaged surface layer in dilute HNO_3

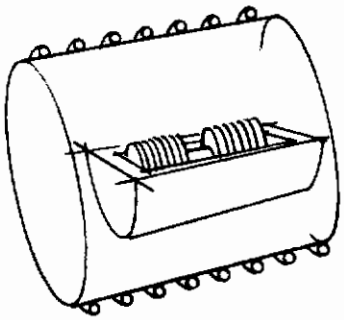

d. Anneal 4 hr. at 900°C 10^{-6} torr in graphite boat

CLEAN AND TIN

e. Clean in dilute HNO_3 and tin ends with soft solder

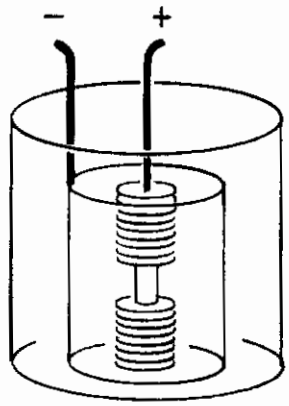

f. Electropolish gage length

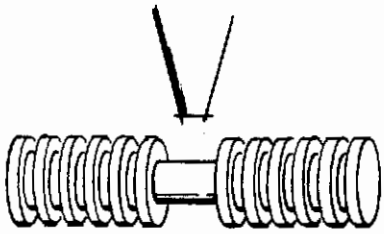

g. Optical measurement of diameter

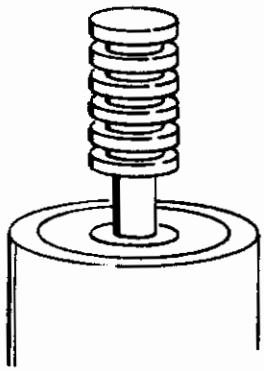

h. Mount specimen in upper grip using tool-makers microscope and cathetometer for alignment. Measure gage length with cathetometer.

MOUNT SPECIMEN

i. Mount specimen and upper grip in Instron

Figure 1 - Procedures for Preparing Fatigue Specimens

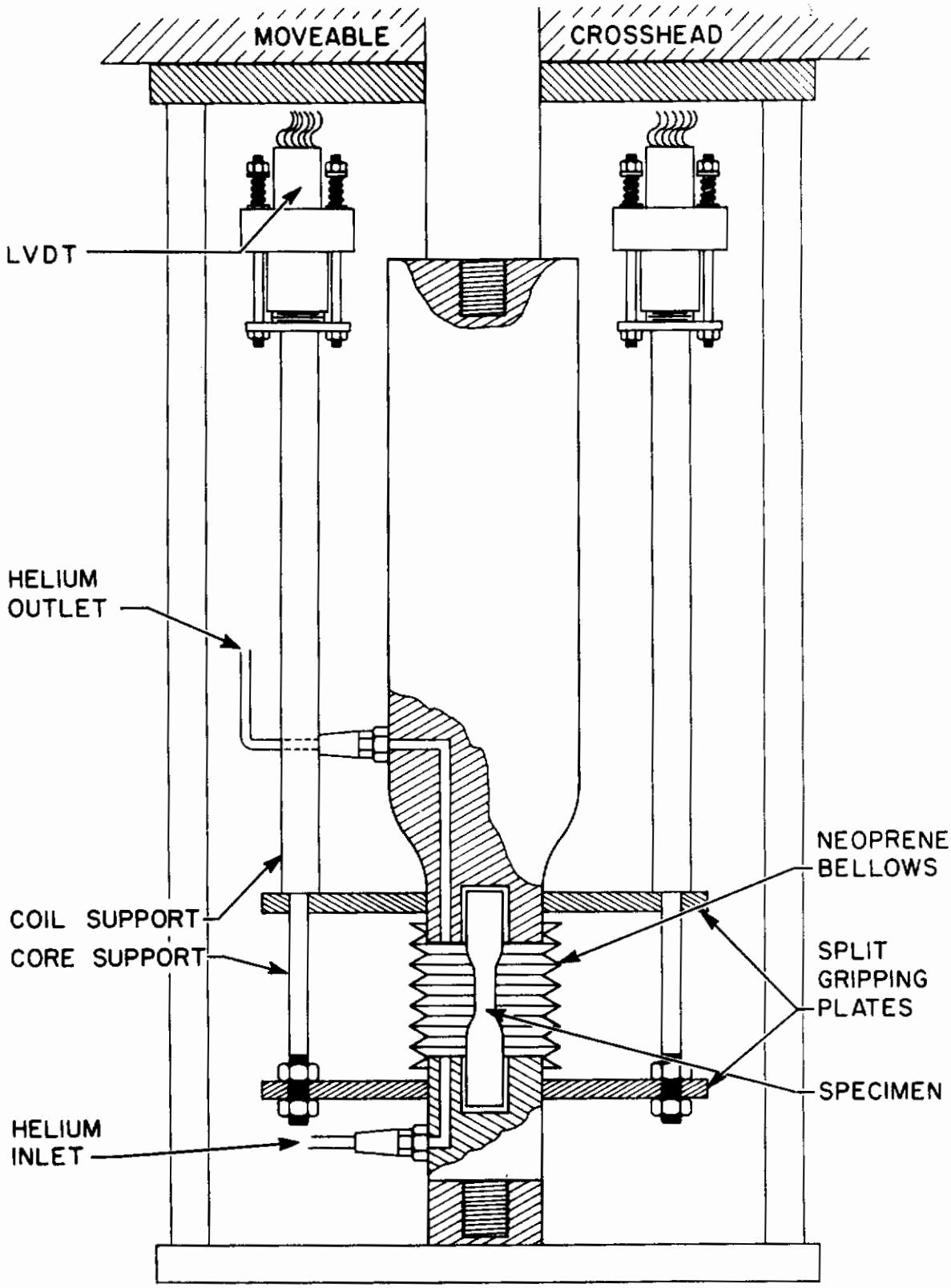

Figure 2 - Assembly for Cyclic Loading on Instron Testing Machine

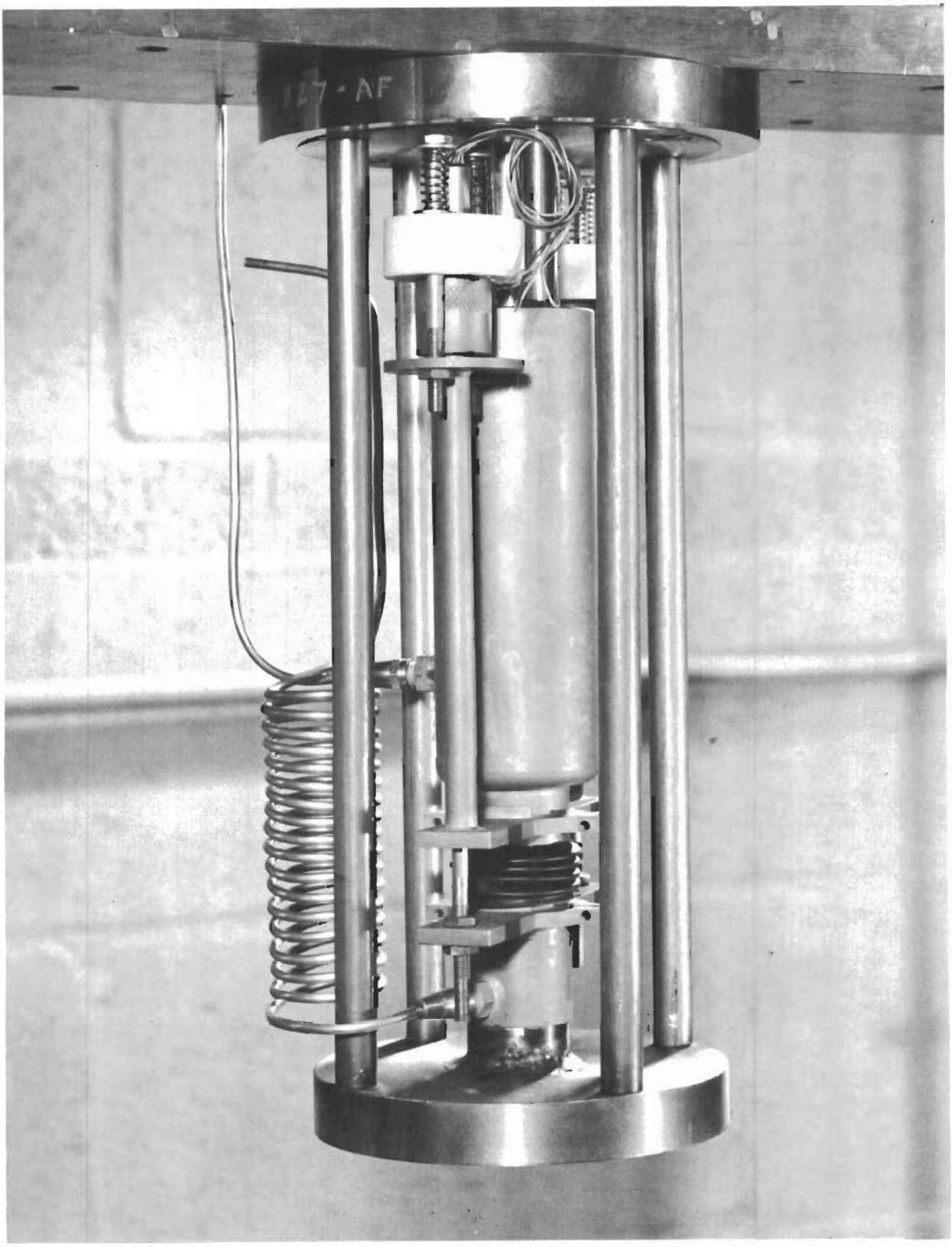

Figure 3 - Loading Fixture and Extensometer Mounted on Instron

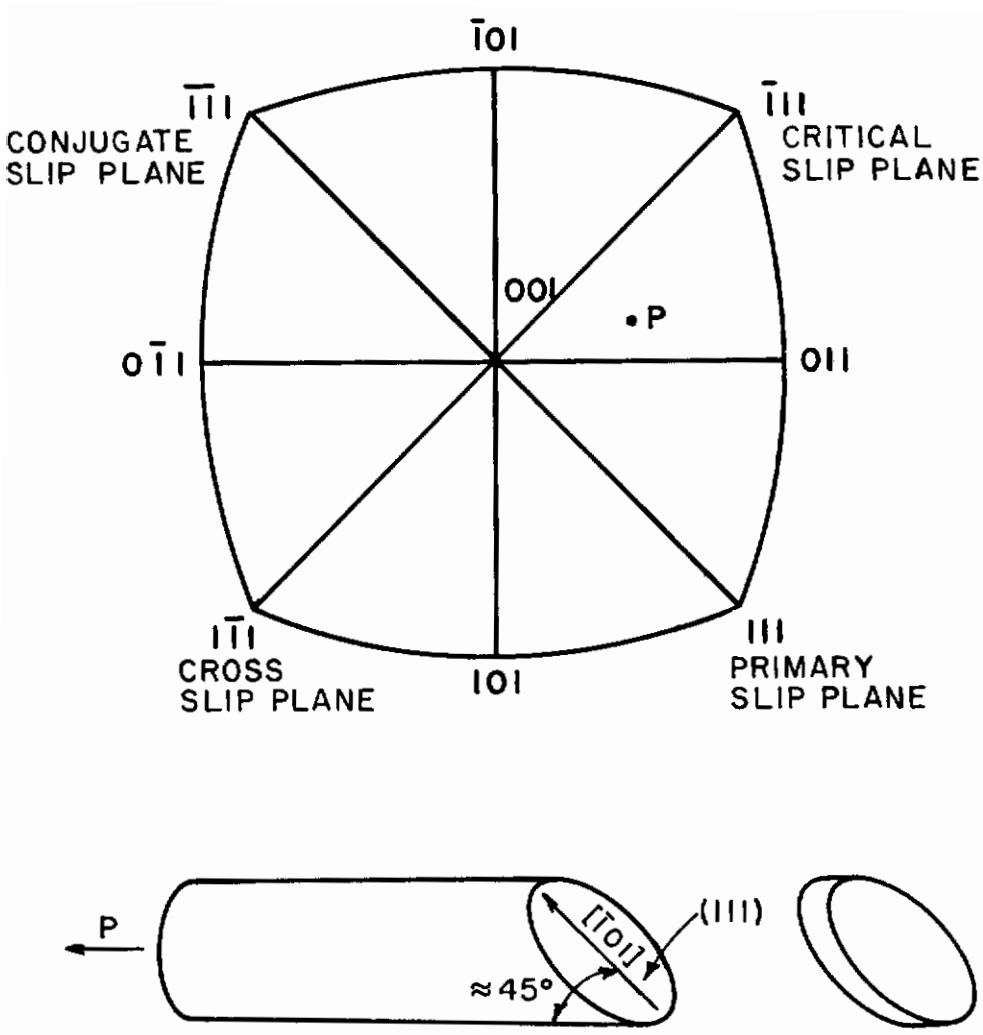

Figure 4 - Copper Single Crystal Orientation and Geometry for Transmission Electron Microscopy

a

Gage Length of Fatigue Specimen

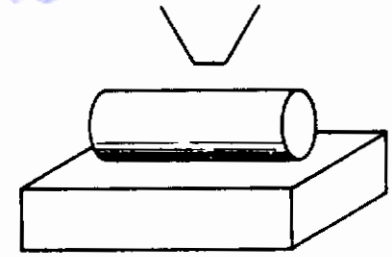

b

Specimen is Oriented and Mounted Under Optical Microscope for Sectioning

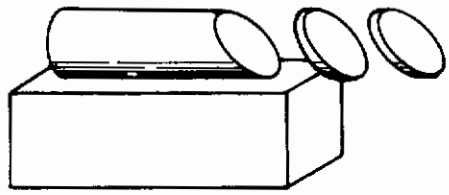

c

Specimen Sectioned Into Disks on Spark-Cutting Machine

d

Indentation is Placed in Disk on Spark-Cutting Machine

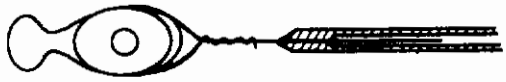

e

Specimen is Mounted in Pt Wire, Gripped with Tweezers, and all Nonessential Areas Insulated with Microstop

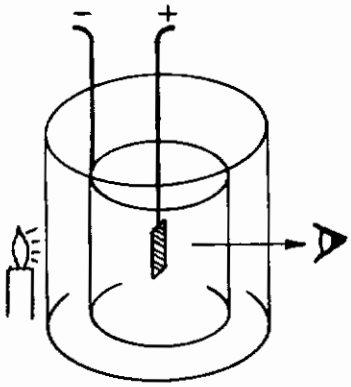

f

Specimen is Electropolished to Transparency

EXAMINATION IN ELECTRON MICROSCOPE

g

Specimen is Examined in the Electron Microscope

Figure 5 - Specimen-Preparation Procedures for Transmission Electron Microscopy

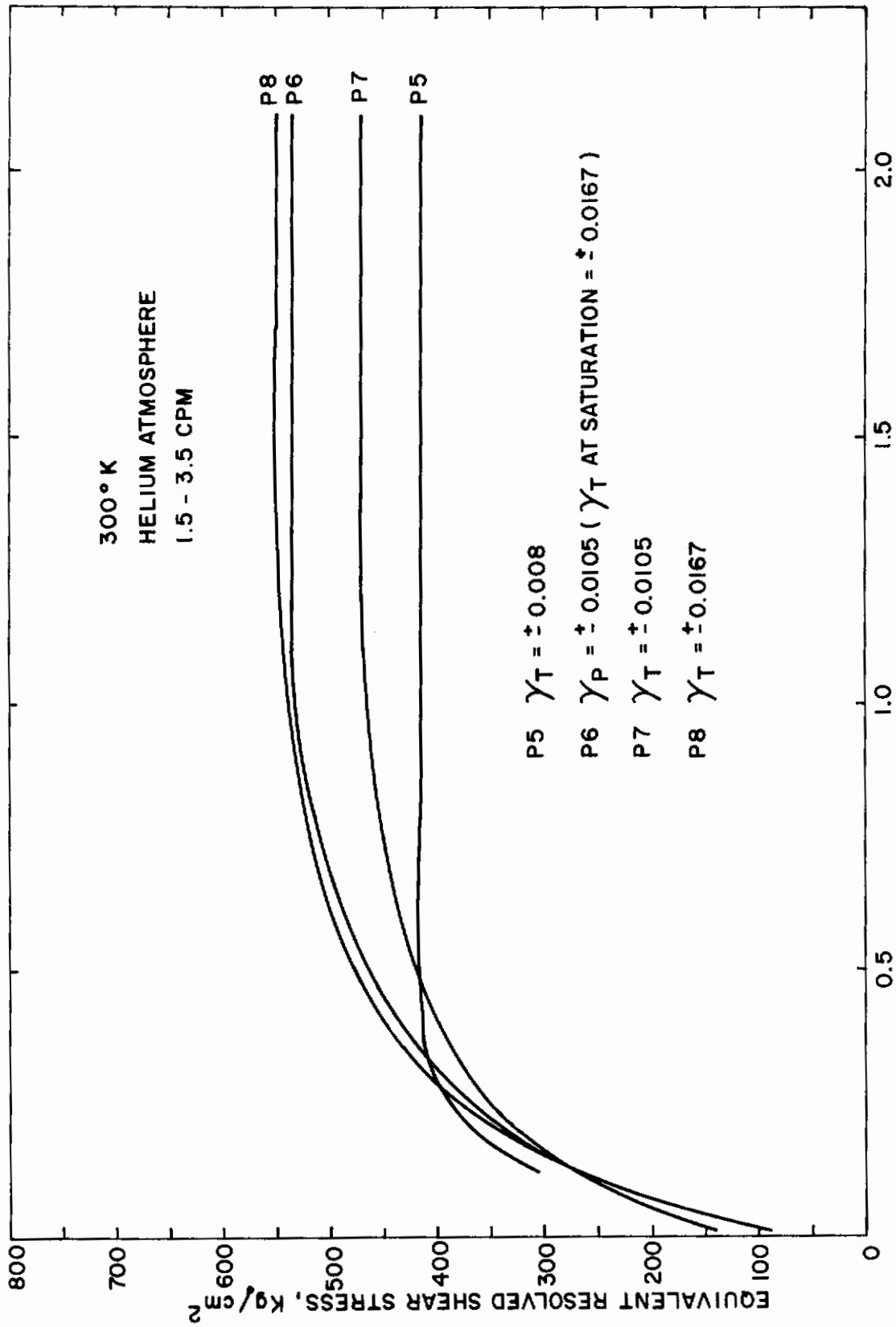

Figure 6 - Cyclic-Strain Hardening Curves for Polycrystalline Copper

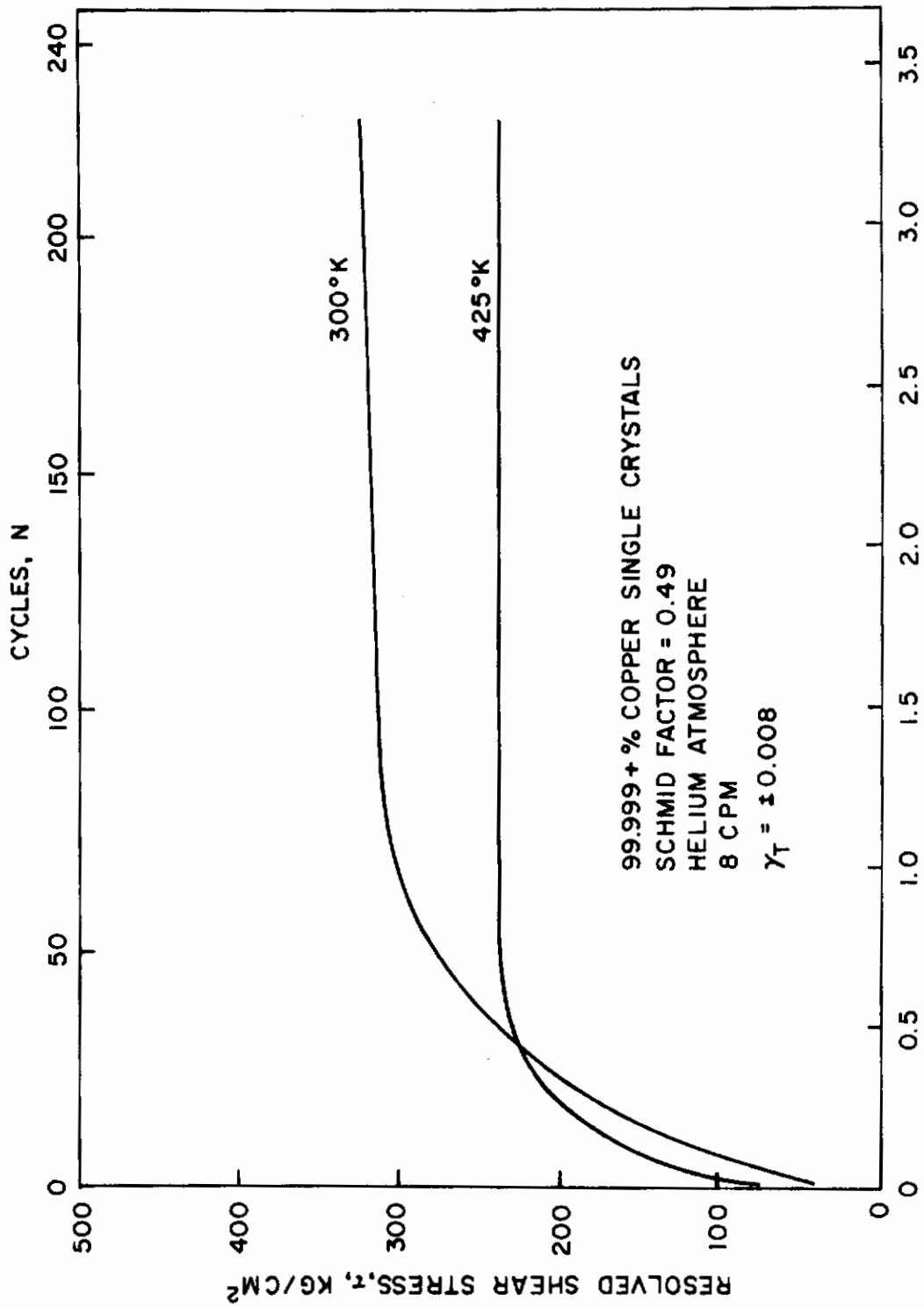

Figure 7 - Cyclic-Strain Hardening Curves for Copper Single Crystals

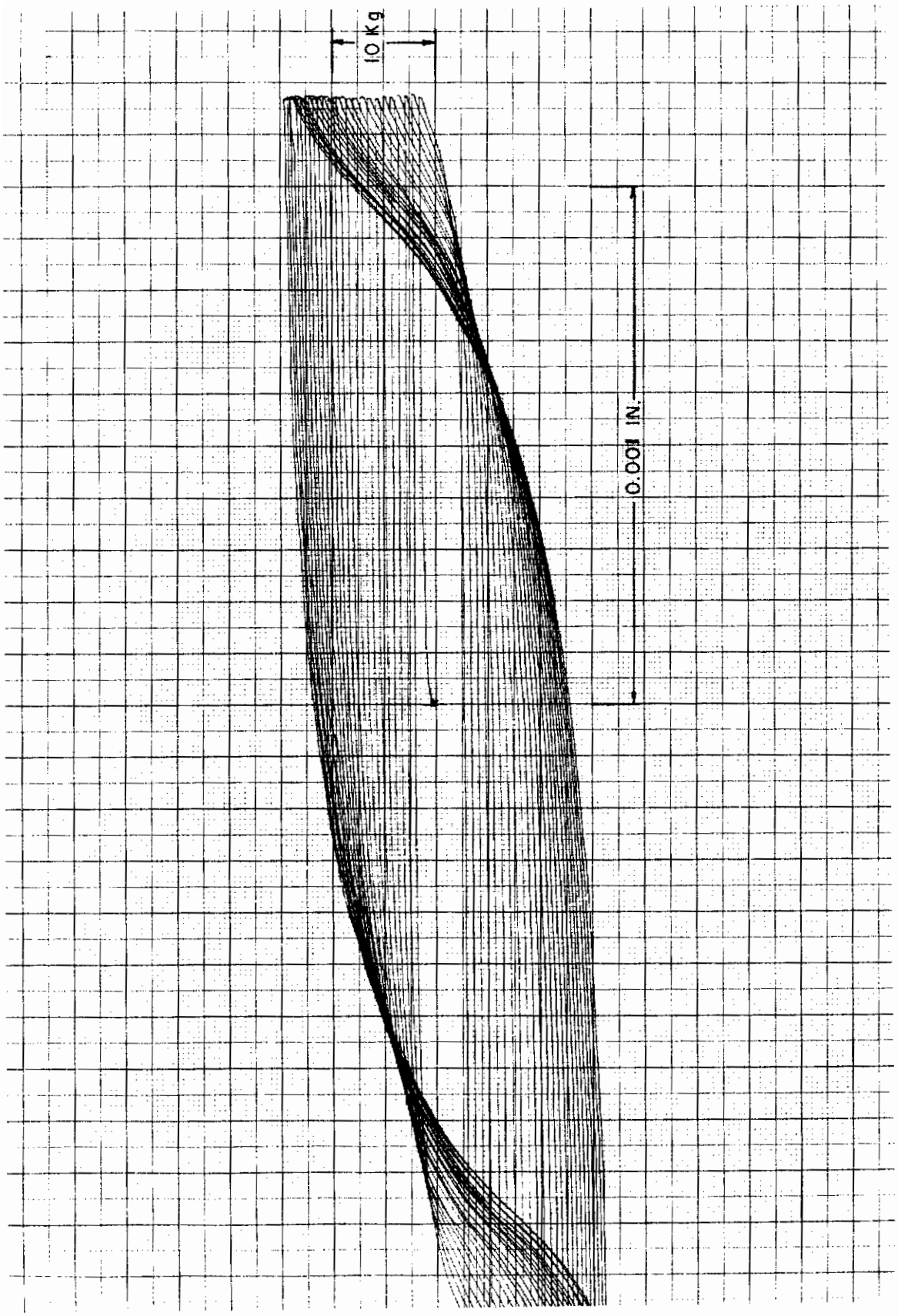

Figure 8 - Load-Extension Plot for Specimen M40 for the First 25 Cycles; $Y_t = \pm 0.008$

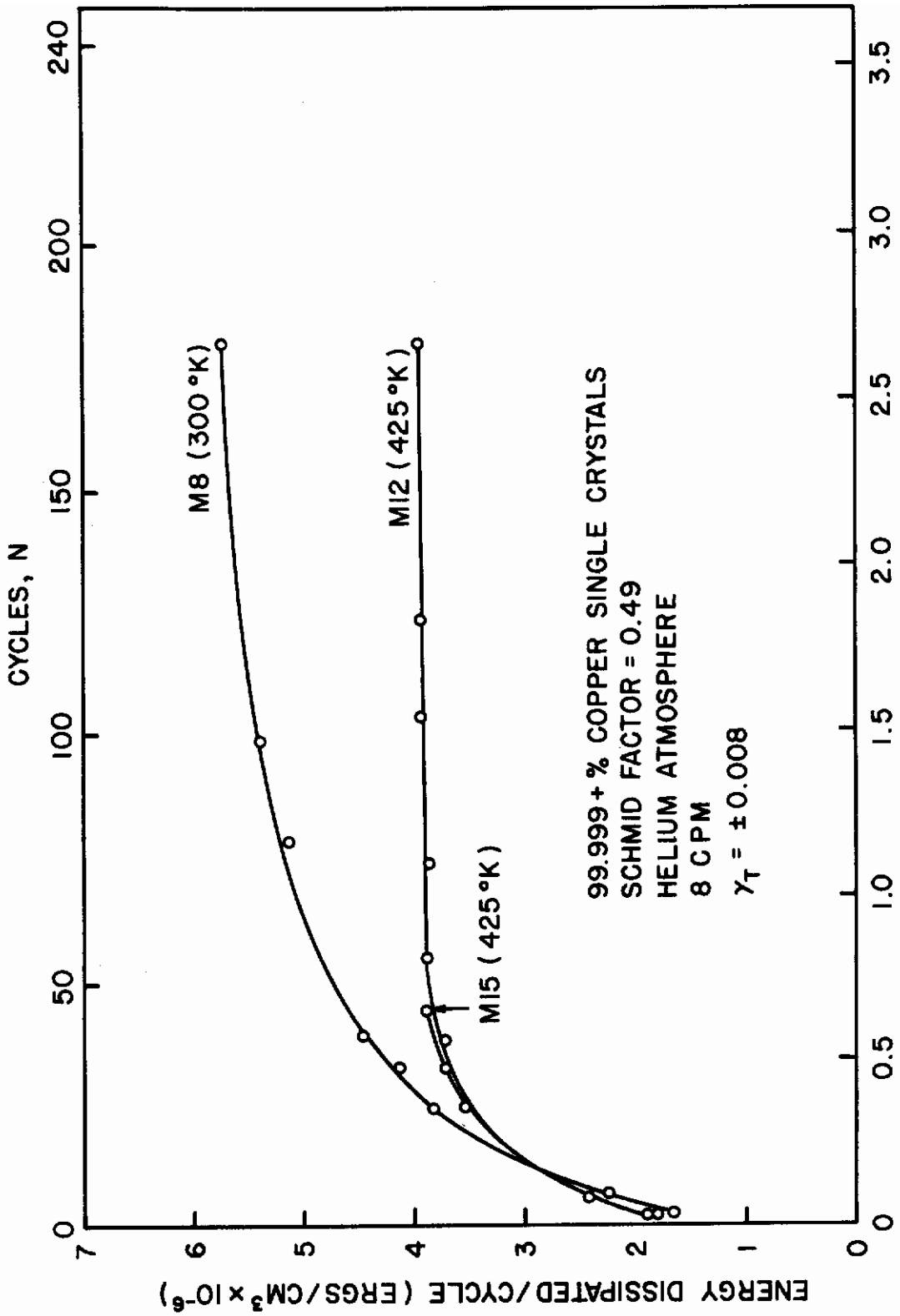

Figure 9 - Specific Energy Dissipated Per Cycle Versus Cumulative Total Shear Strain for Copper Single Crystals

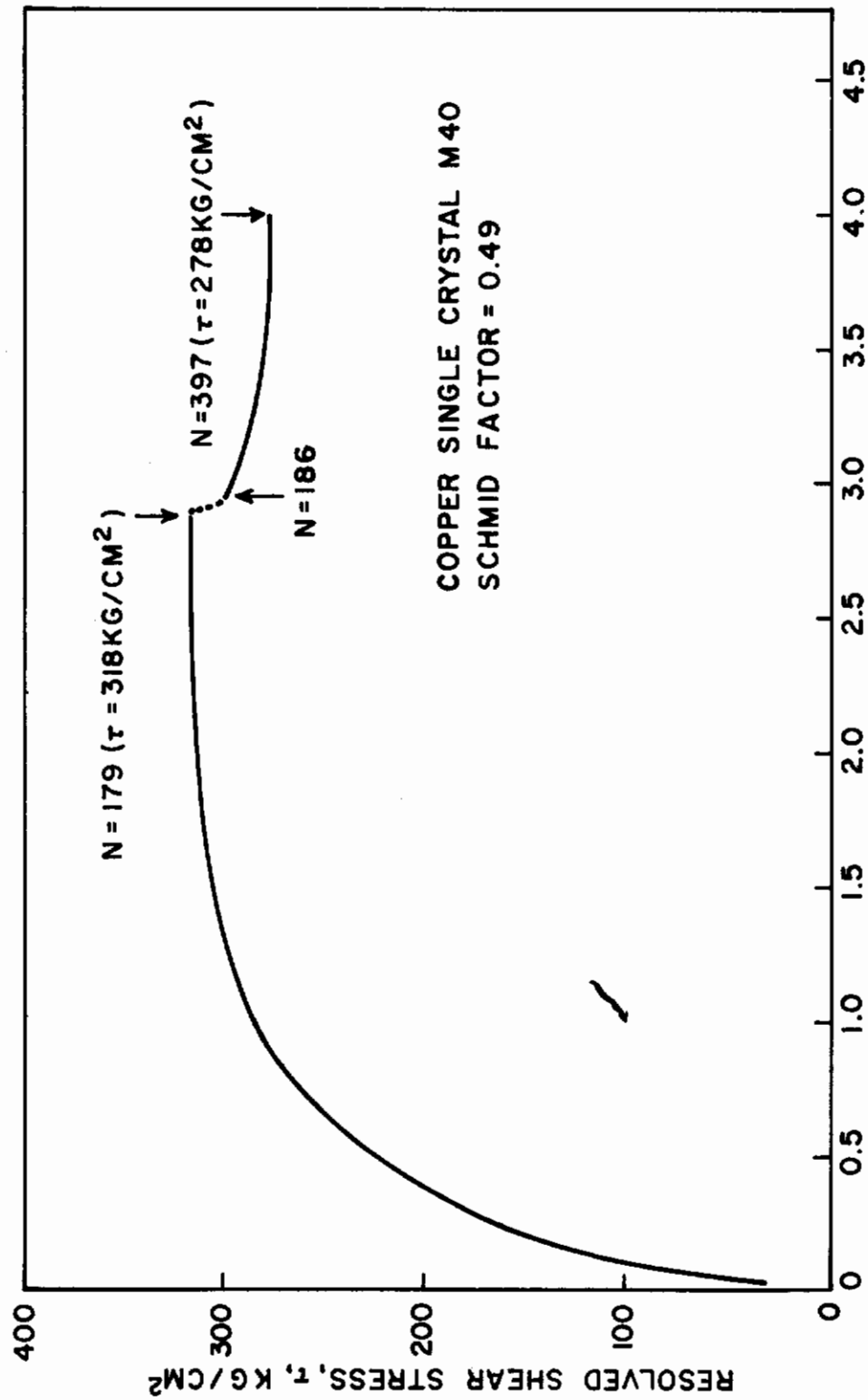

Figure 10 - Cyclic-Strain Hardening ($\gamma_t = \pm$ 0.008; 8 cpm) and Softening ($\gamma_t = \pm$ 0.0025; 10 cpm) for a Copper Single Crystal (M40)

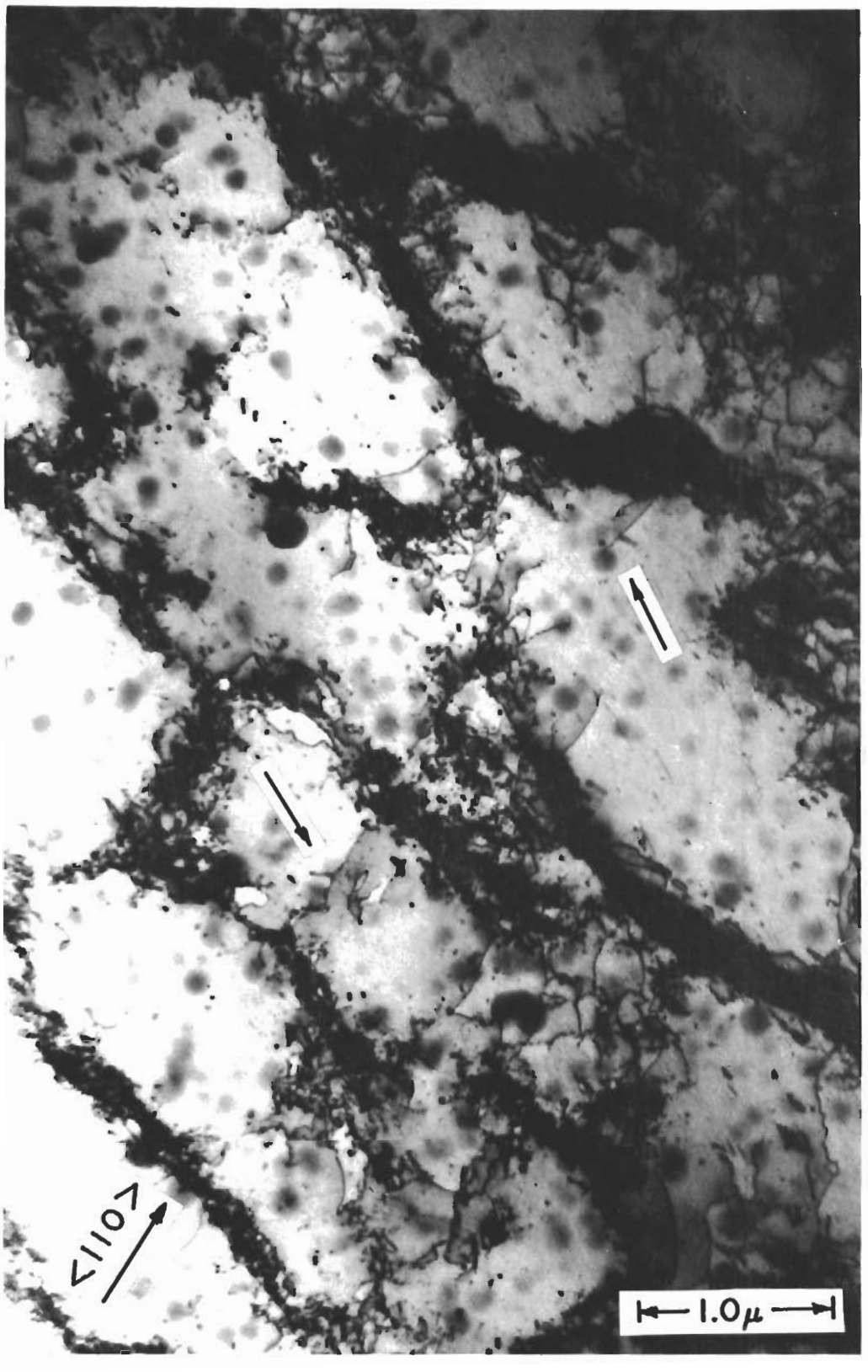

Figure 11 - Dislocation Arrangements in Polycrystalline Specimen P5. Cell walls aligned in <110> directions; dipole formation is indicated by arrows. $\gamma_t = \pm 0.008$, 300°K, N = 410, τ_{Sat} = 416 kg/cm^2.

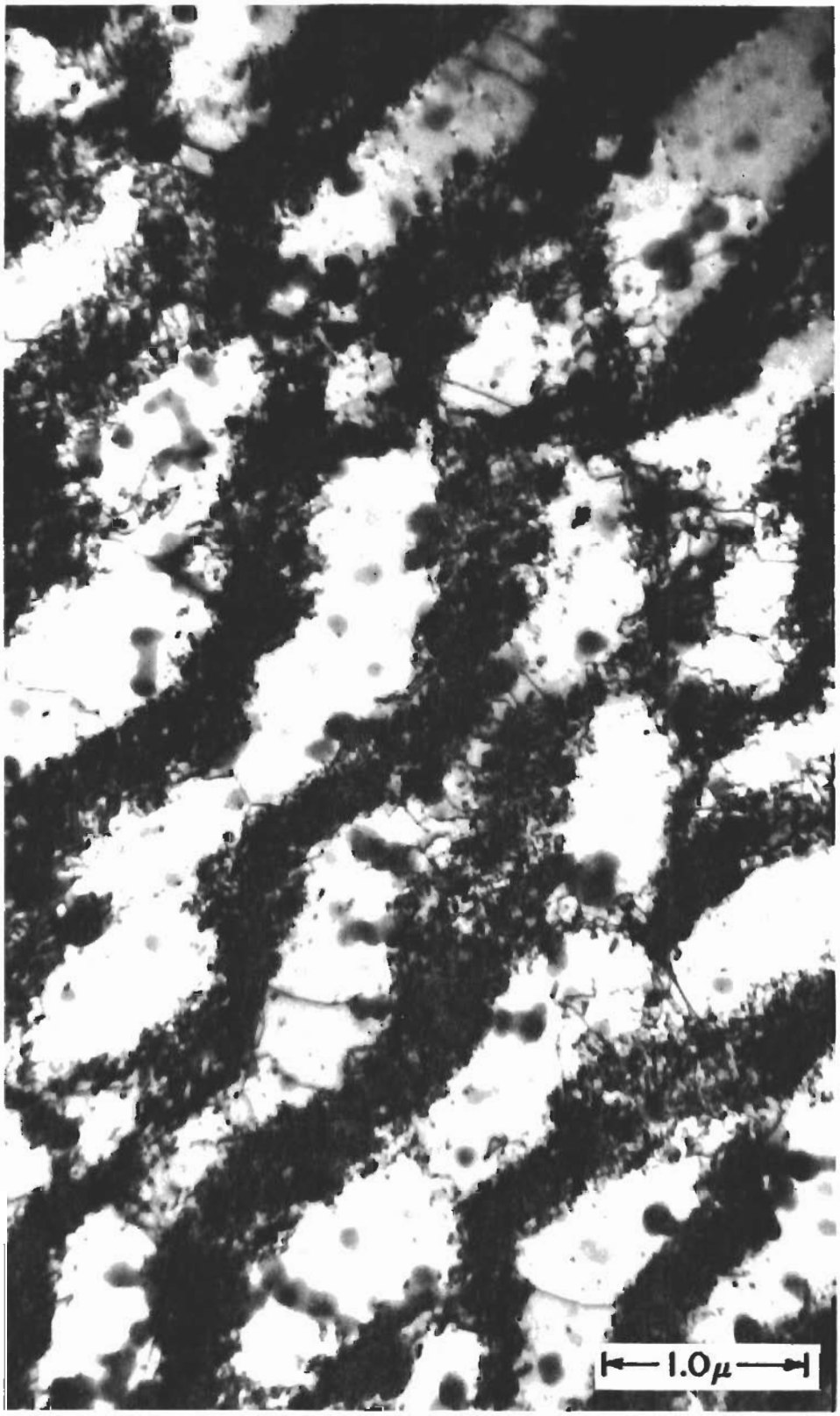

Figure 12 - Dislocation Arrangements in Polycrystalline Specimen P6. $\gamma_P = \pm 0.0105$, 300°K, N = 330, $\tau_{Sat.} = 535$ kg/cm^2.

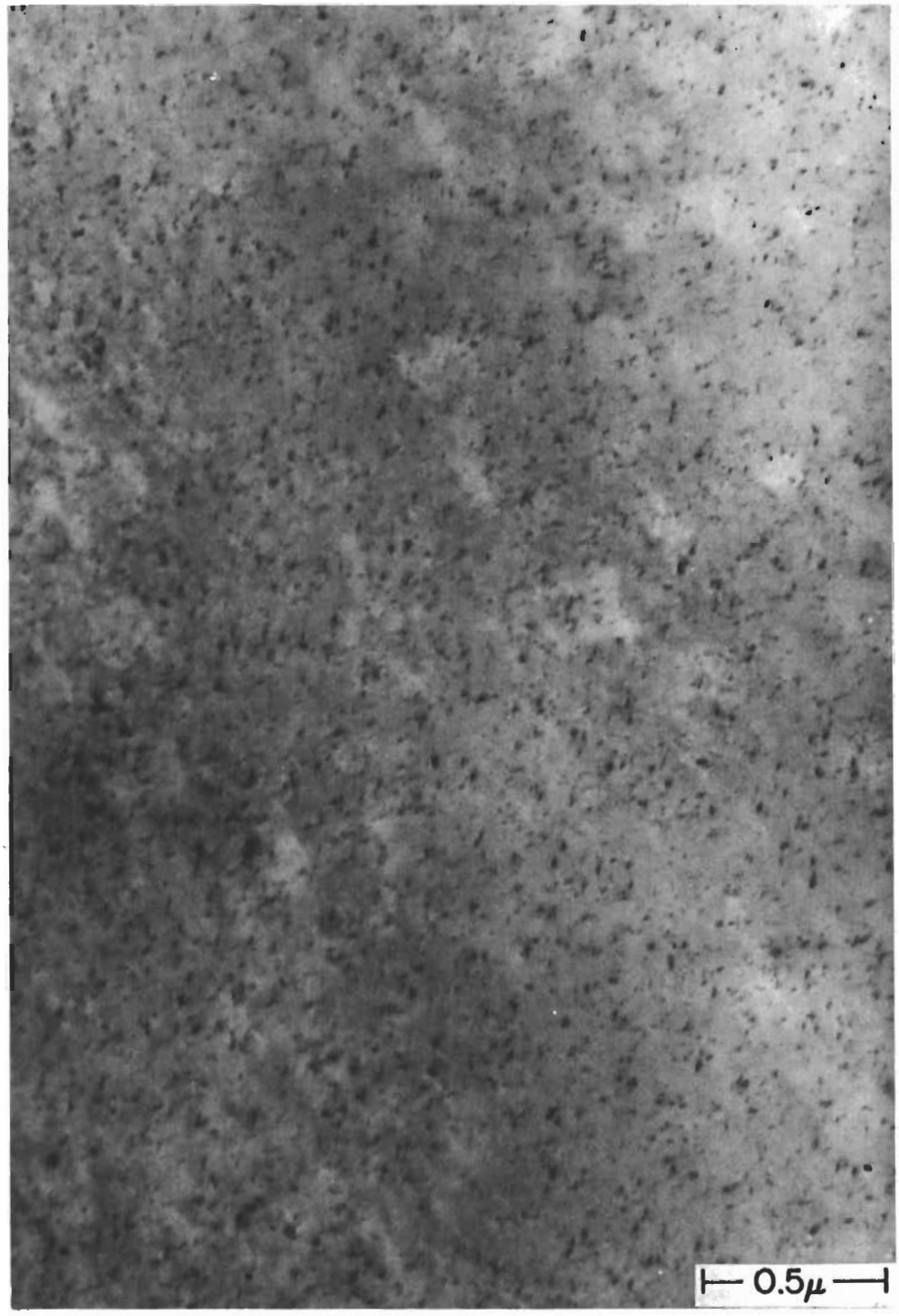

(A)

Figure 13 - Copper Single Crystal (M10) Annealed 4 Hr. at 1220°K and Irradiated with Fast Neutrons (> 0.4 Mev) to 1.37 x 10^{18} nvt

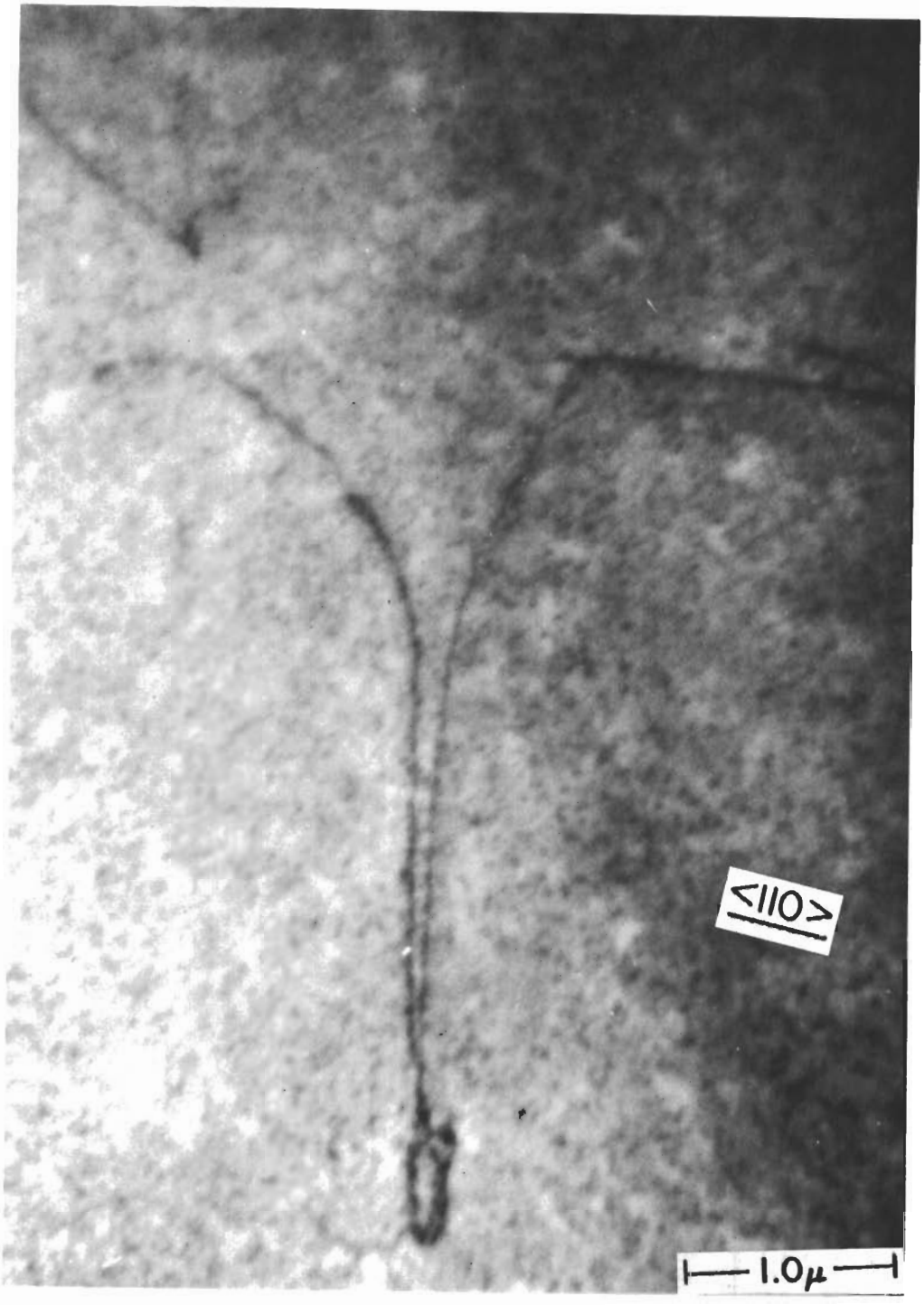

(B)

Figure 13 (Concluded)

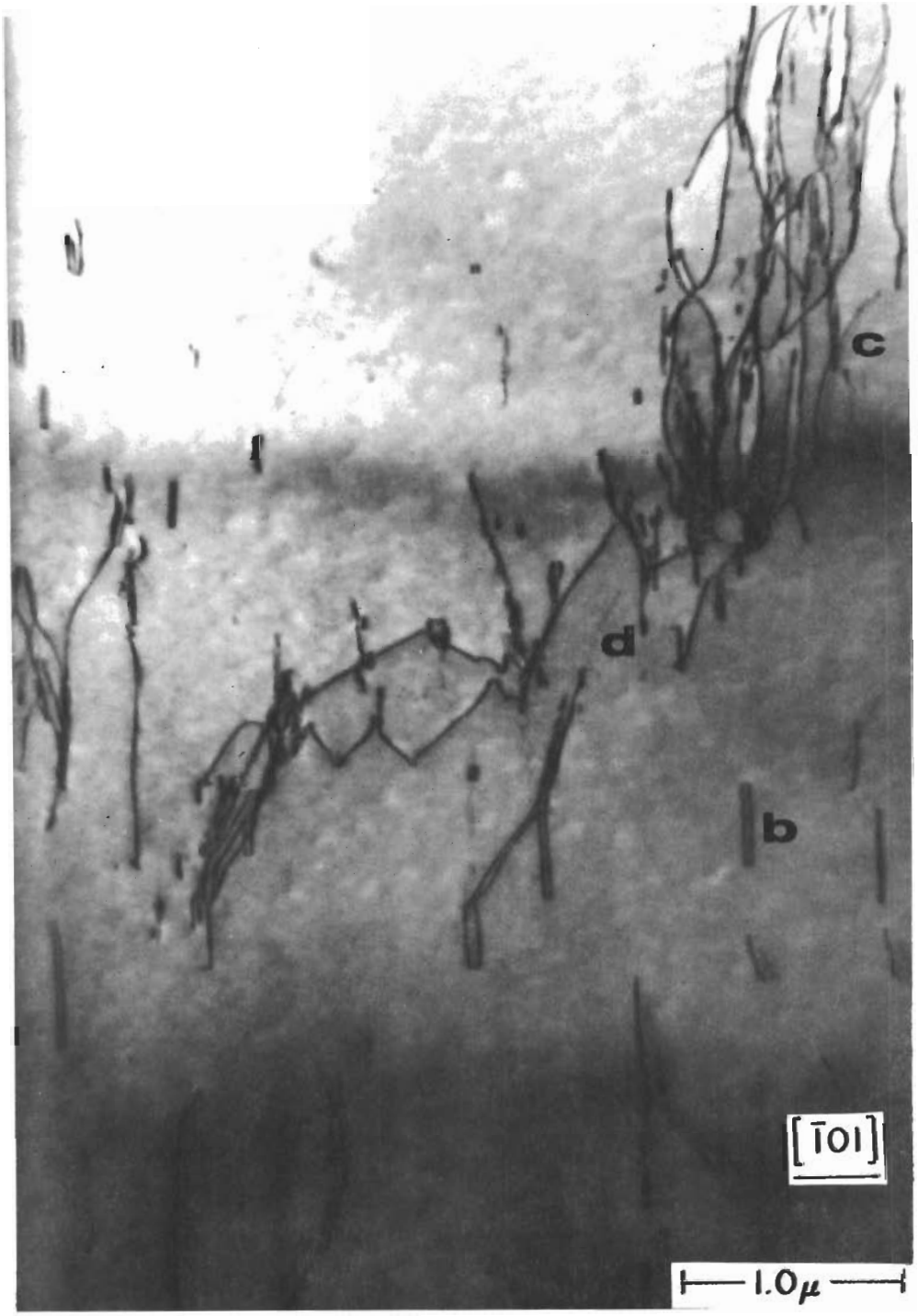

(A)

Figure 14 - Dislocation Arrangements in Single Crystal M36, N = 4-1/2. The primary Burgers vector is ± [101]; (A) = [0$\bar{2}$2]; examples of prismatic closed-loop dipoles at (b), bundles of edge dislocations at (c), and Frank partial dislocations at (d) are shown; (B) a prismatic closed-loop dipole is shown at (b), and bundles of edge dislocations are shown at (c).

(B)

Figure 14 (Concluded)

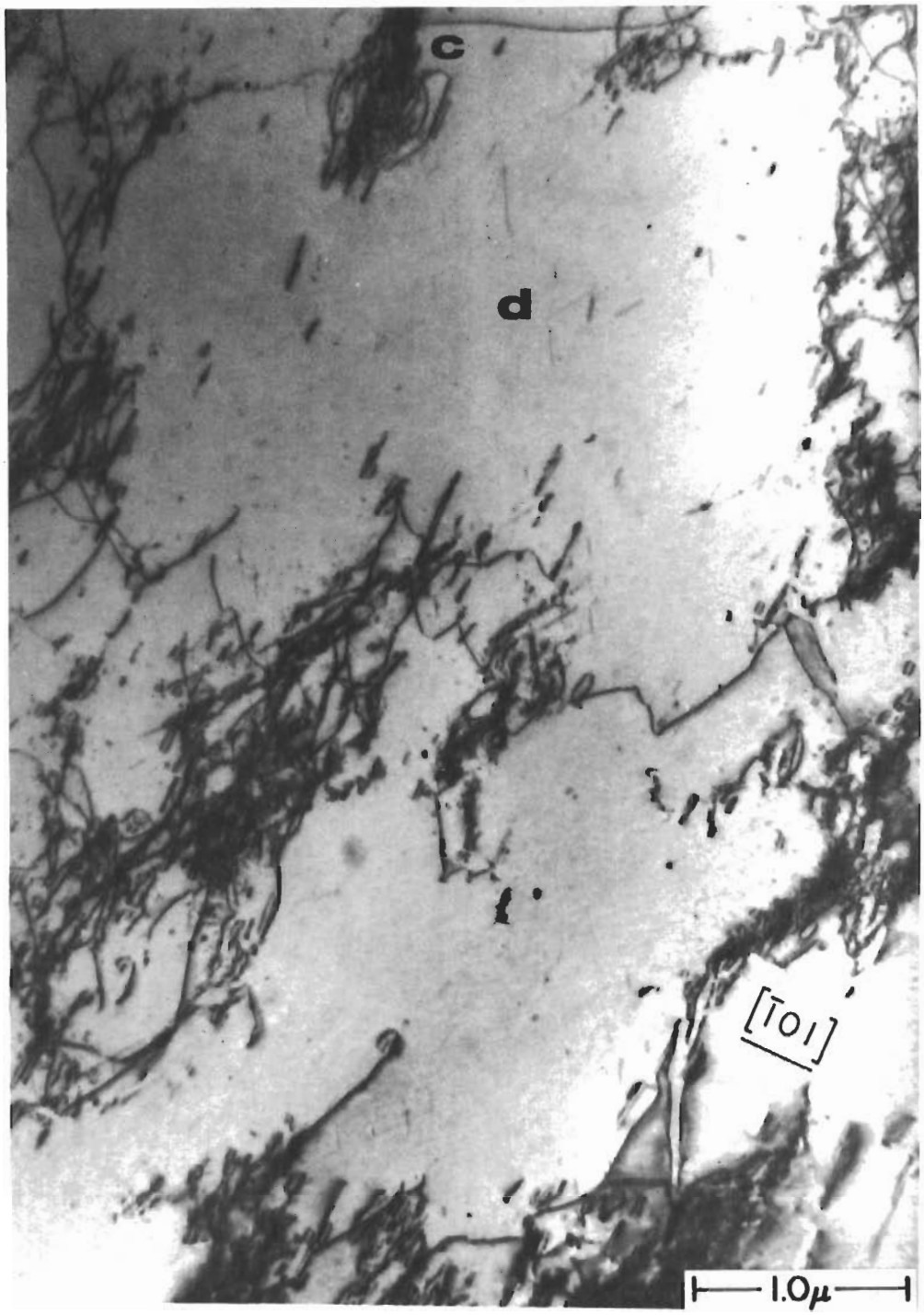

(A)

Figure 15 - Dislocation Arrangements in Single Crystal M22, N = 20. The primary Burgers vector is the ± [$\bar{1}$01] direction; (A) g = [20$\bar{2}$] and [$\bar{1}\bar{1}$3]; bundles of edge dislocations are shown at (c), and Frank partials at (d); (B) g = 220 ; a prismatic closed-loop dipole is shown at (b).

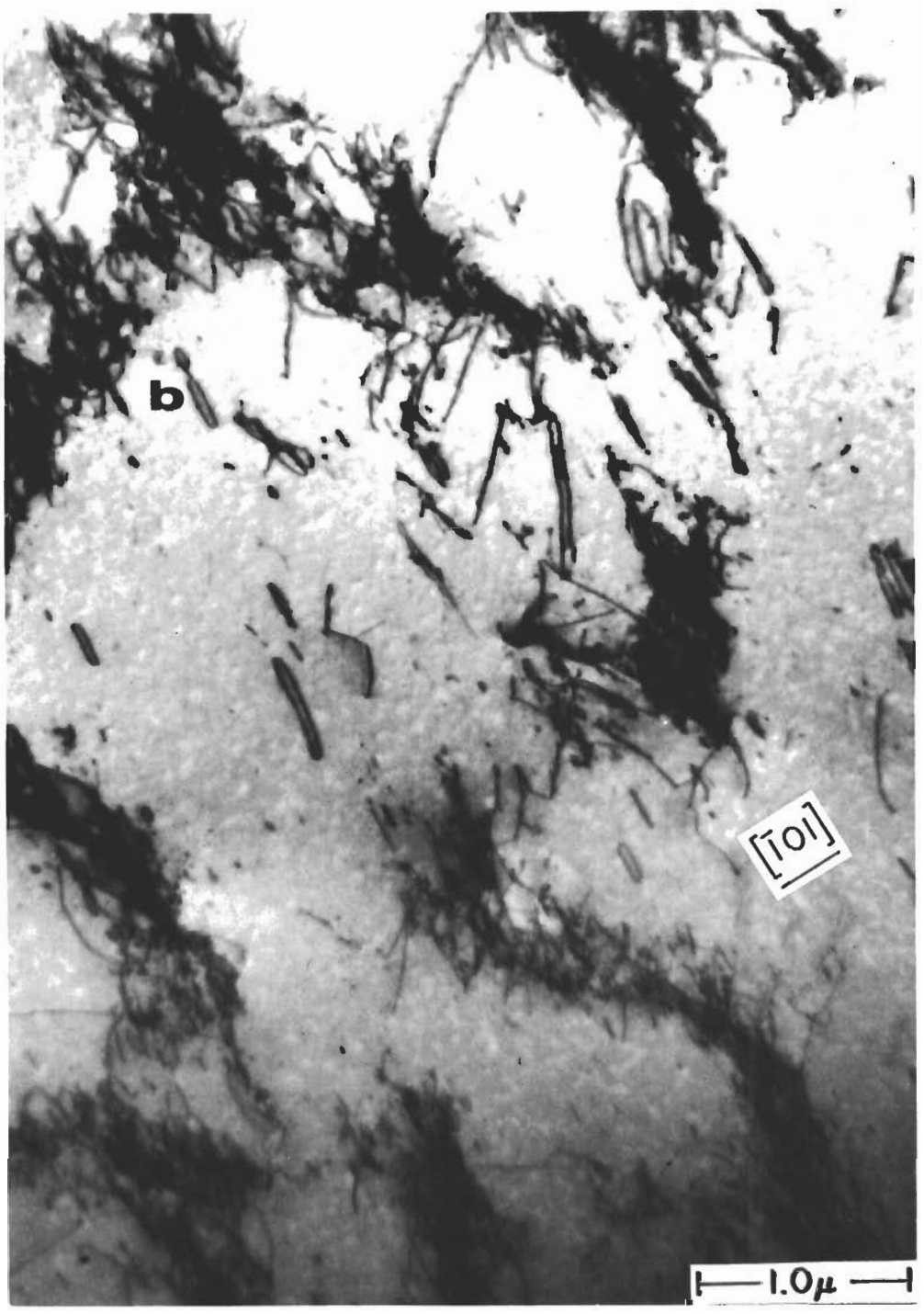

(B)

Figure 15 (Concluded)

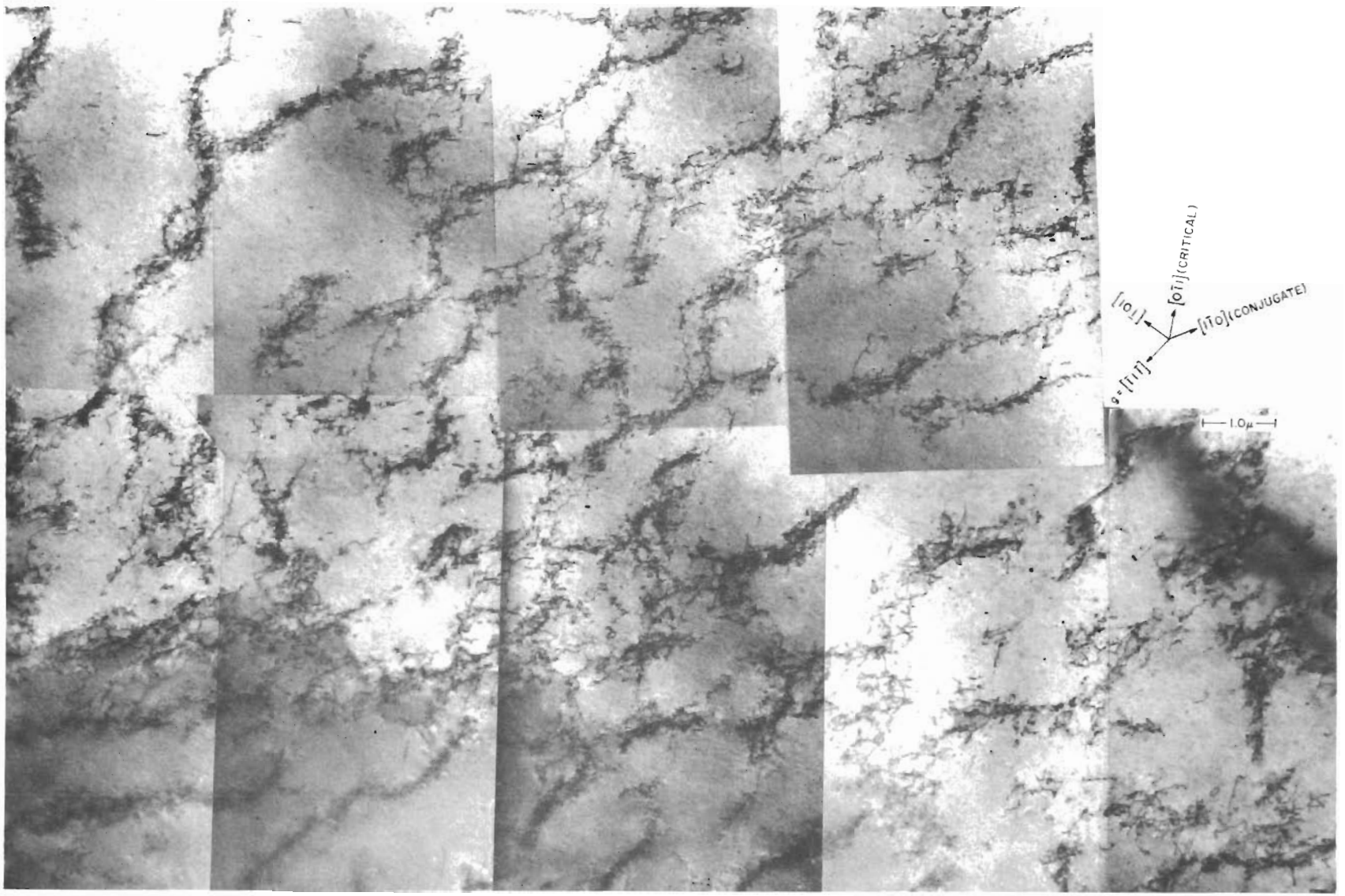

(A)

Figure 16 - Dislocation in (A) Single Crystal M34; N = 100; g = $[\bar{1}1\bar{1}]$; and (B) Single Crystal M4 (Irradiated); N = 100; g = $[\bar{2}0\bar{2}]$.

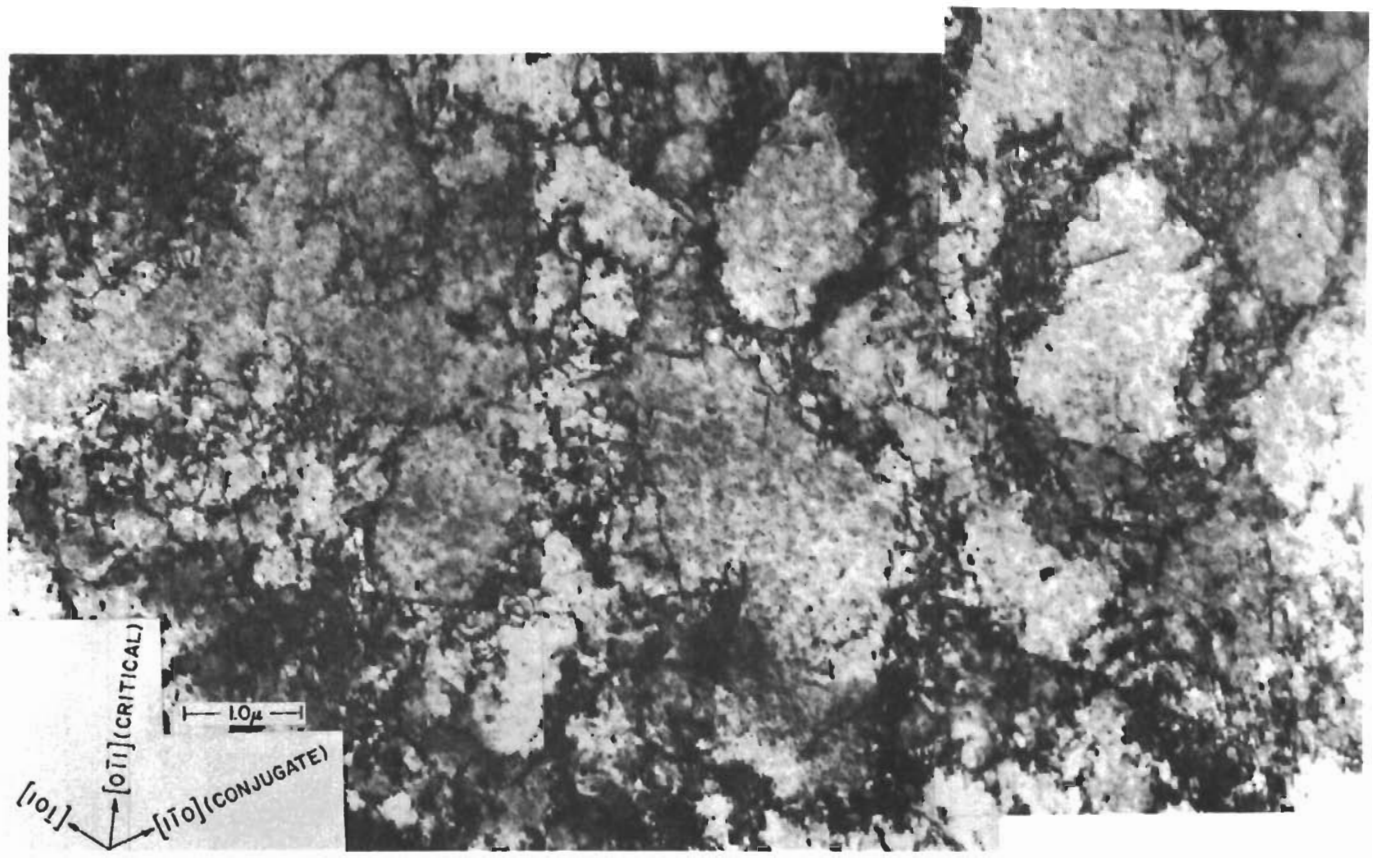

(B)

Figure 16 (Concluded)

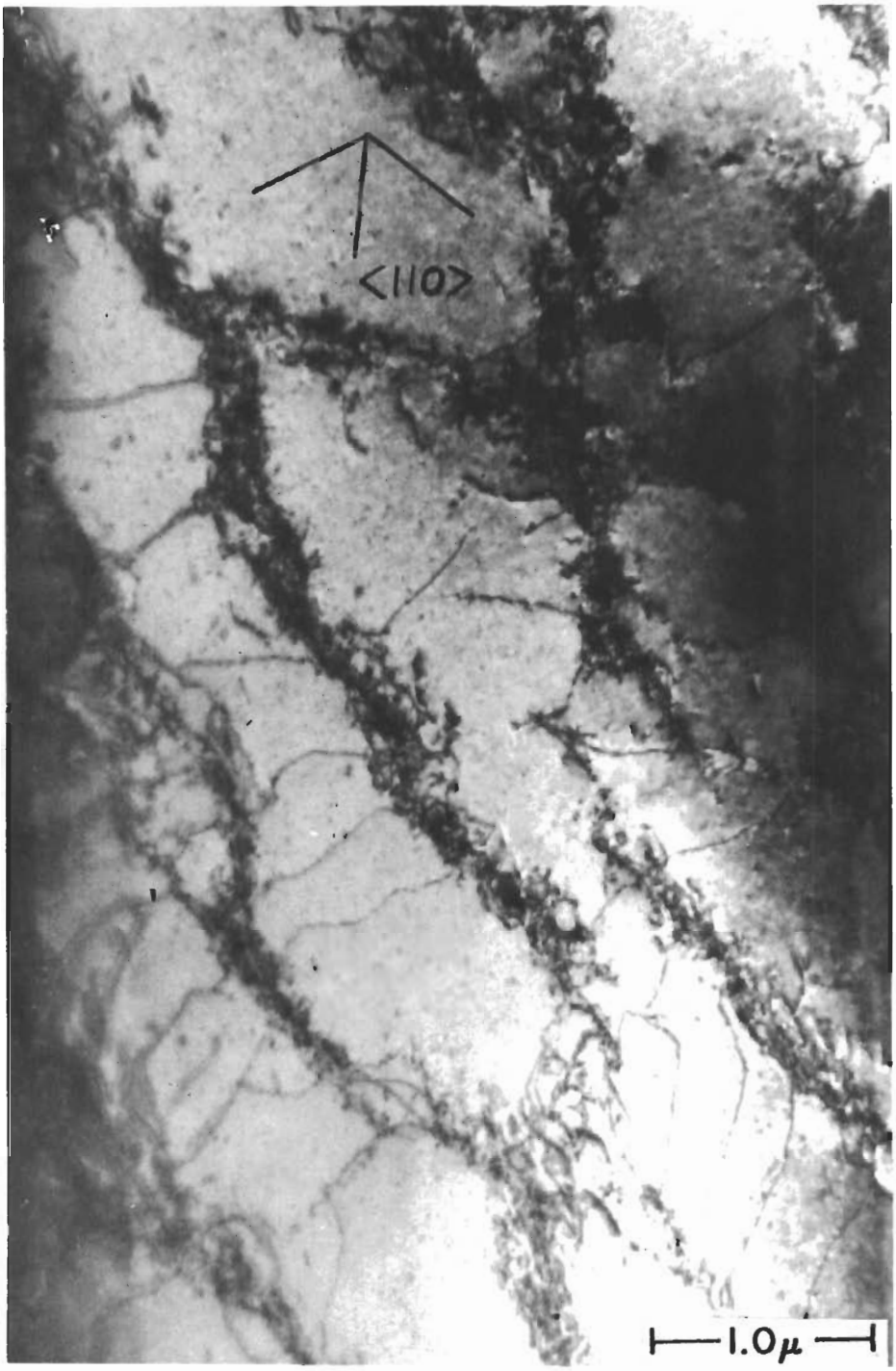

(A)

Figure 17 - Dislocation Arrangements in Single Crystal M8 (Irradiated); N = 660; zone axis = [111]; $g = [0\bar{2}2]$ for (A).

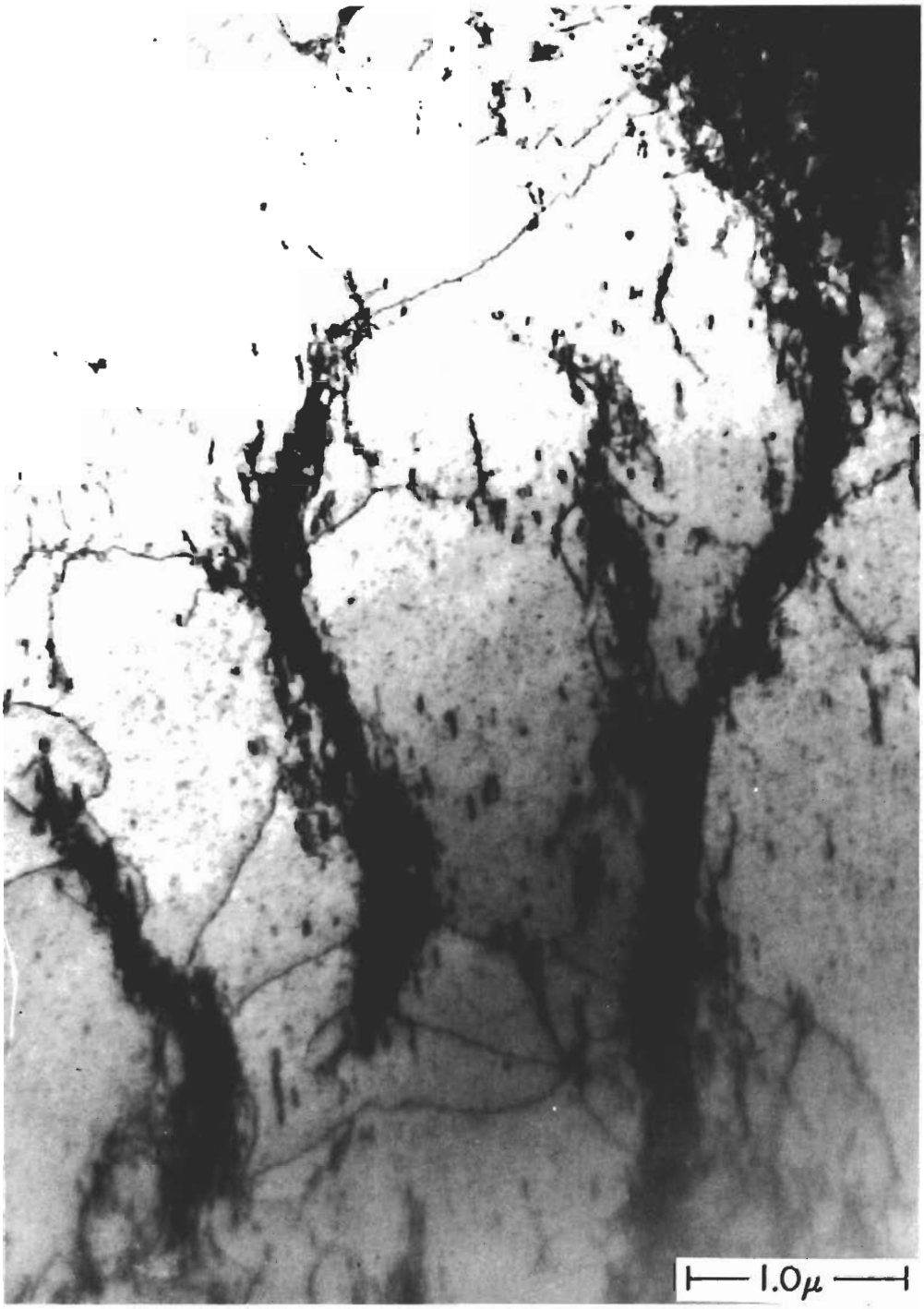

(B)

Figure 17 (Concluded)

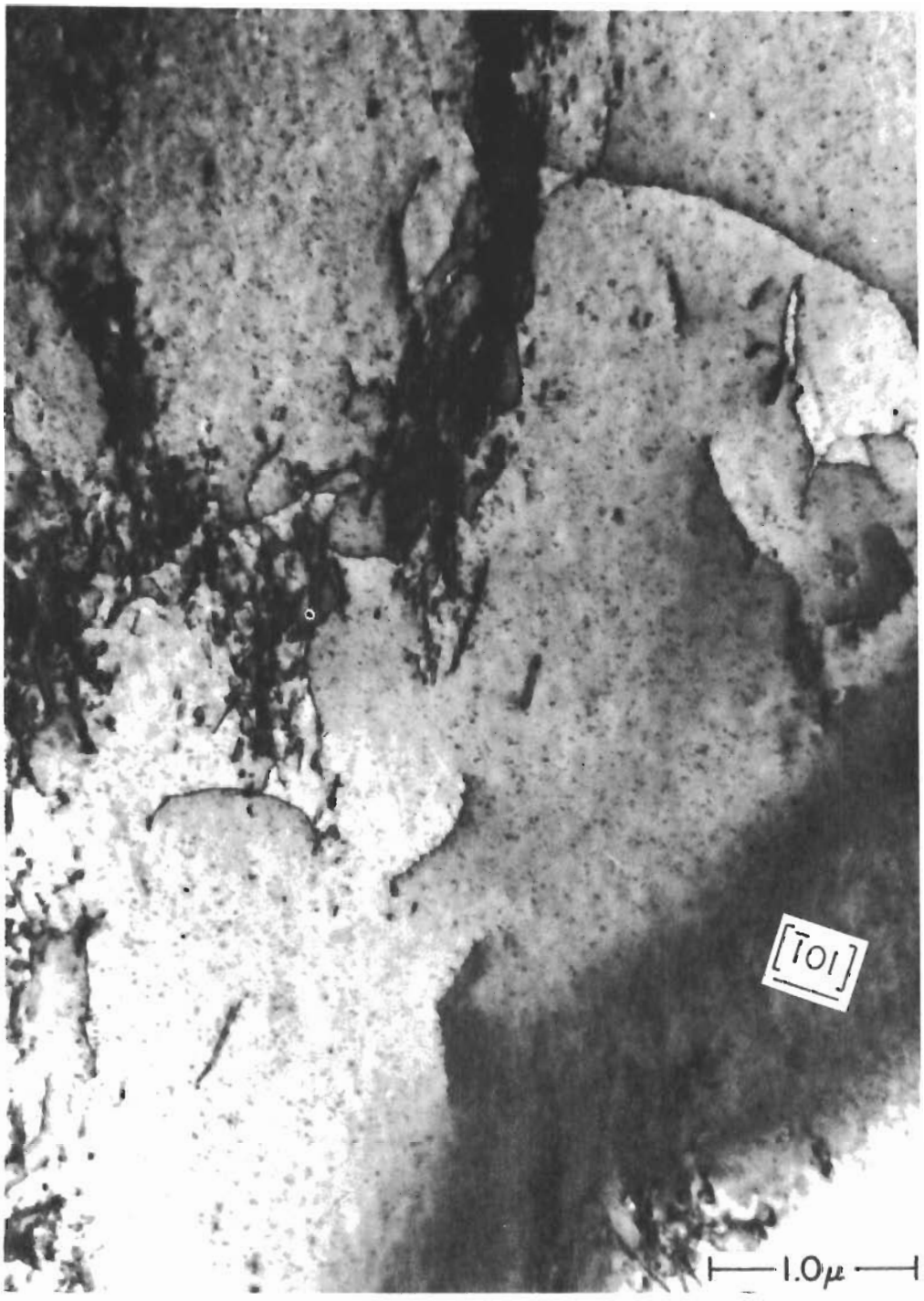

Figure 18 - Copper Single Crystal M6 (Irradiated); N = 20. Isolated dislocations in an irradiated specimen.

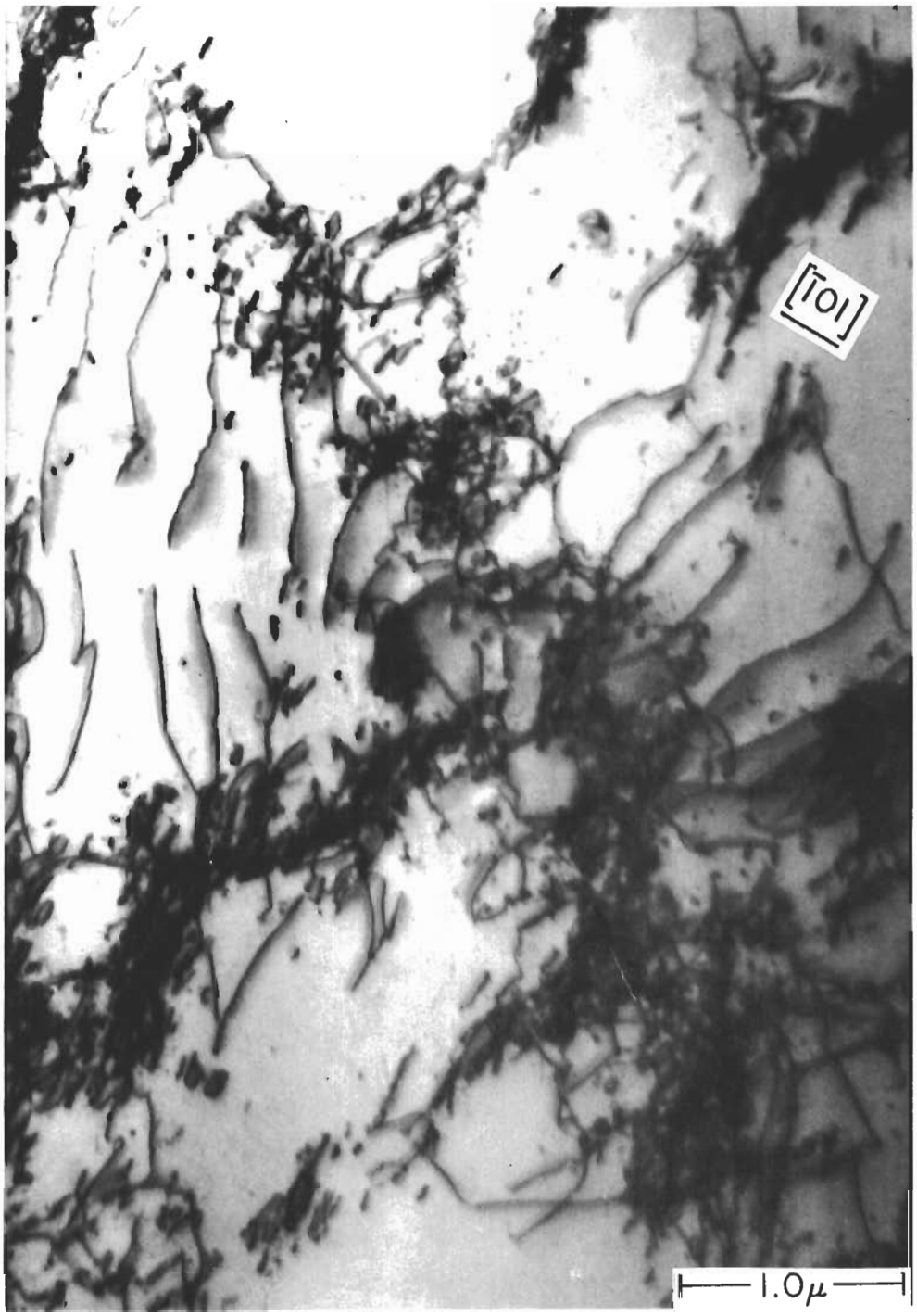

Figure 19 - Copper Single Crystal M22; N = 20. Example of isolated dislocations in an unirradiated specimen.

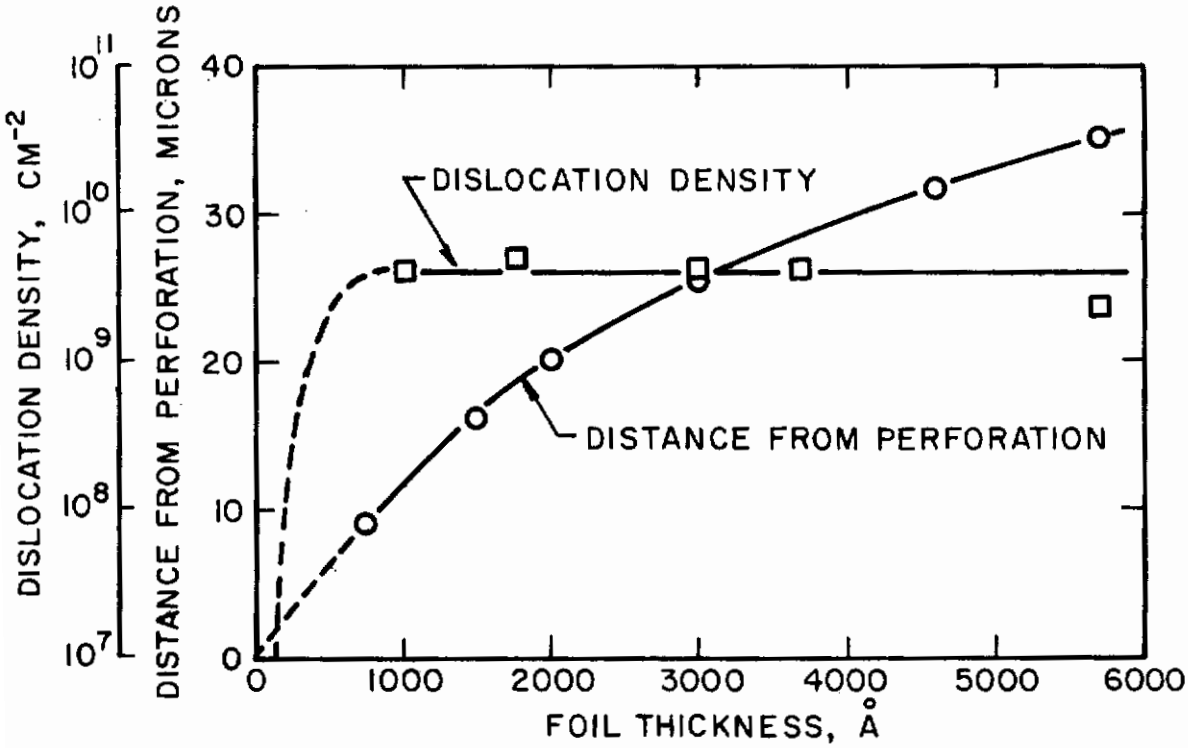

Figure 20 - Profile of Foil Thickness and Dislocation Density in Crystal M22 (Unirradiated)

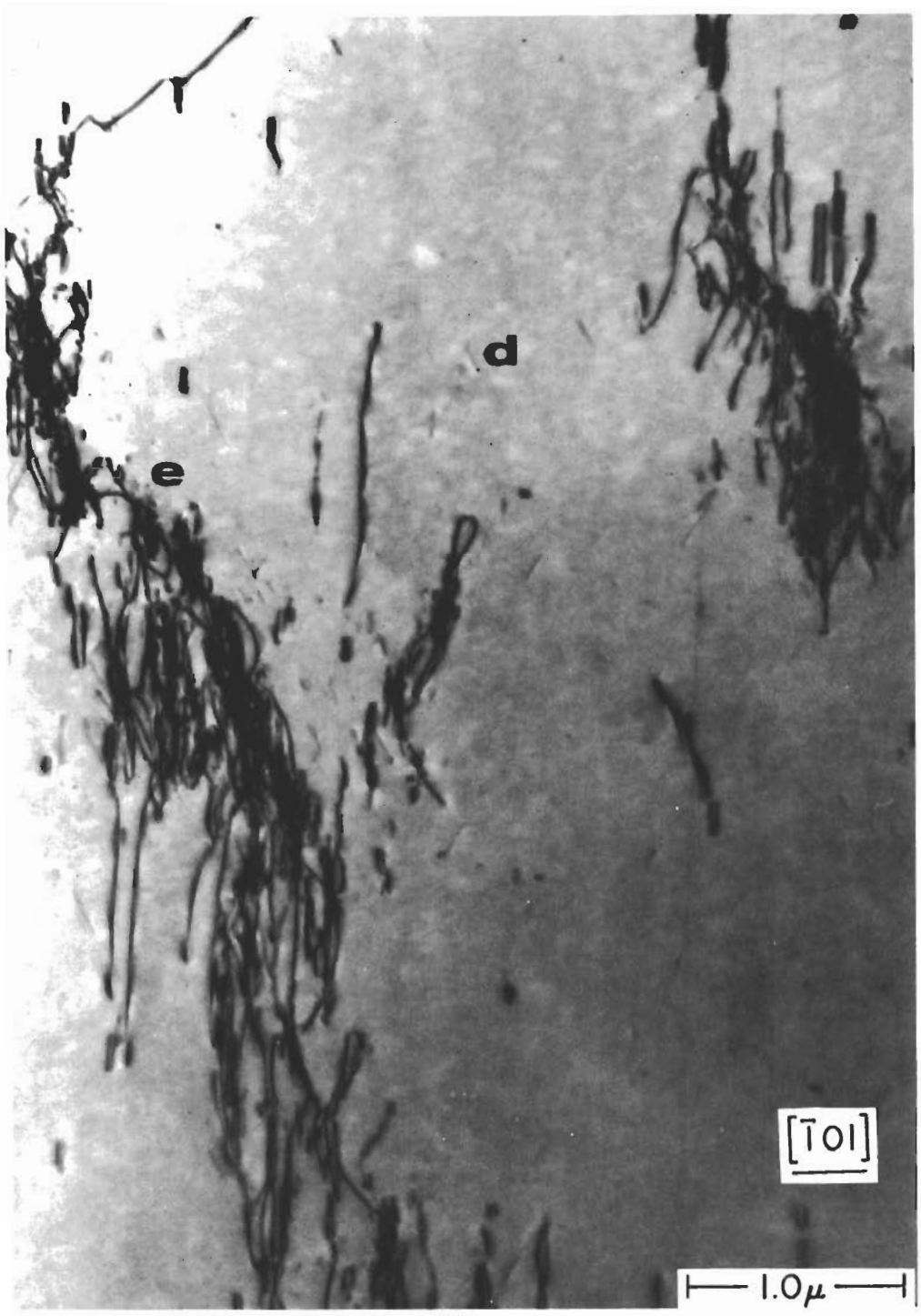

(A)

Figure 21 - Dislocation Arrangements in Single Crystal M36 After 4-1/2 Cycles. Zone axis = [111], g = primary <220> directions. Frank partial dislocations are shown at (d) and the alignment of cell walls and dislocations along the traces of the conjugate and critical slip planes in association with Frank partials are shown at (e). Prismatic dipoles are being formed at (f) in (C).

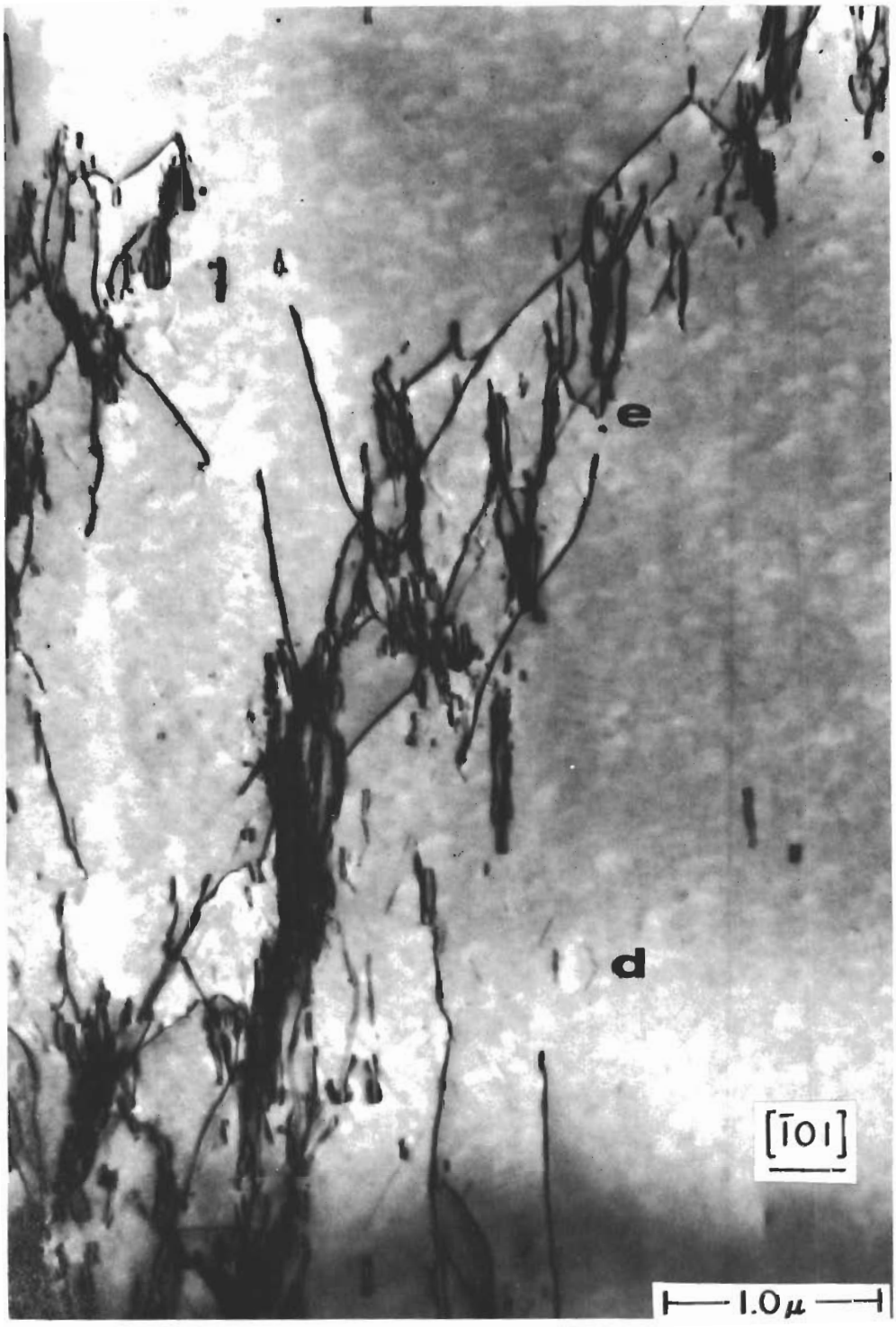

(B)

Figure 21 (Continued)

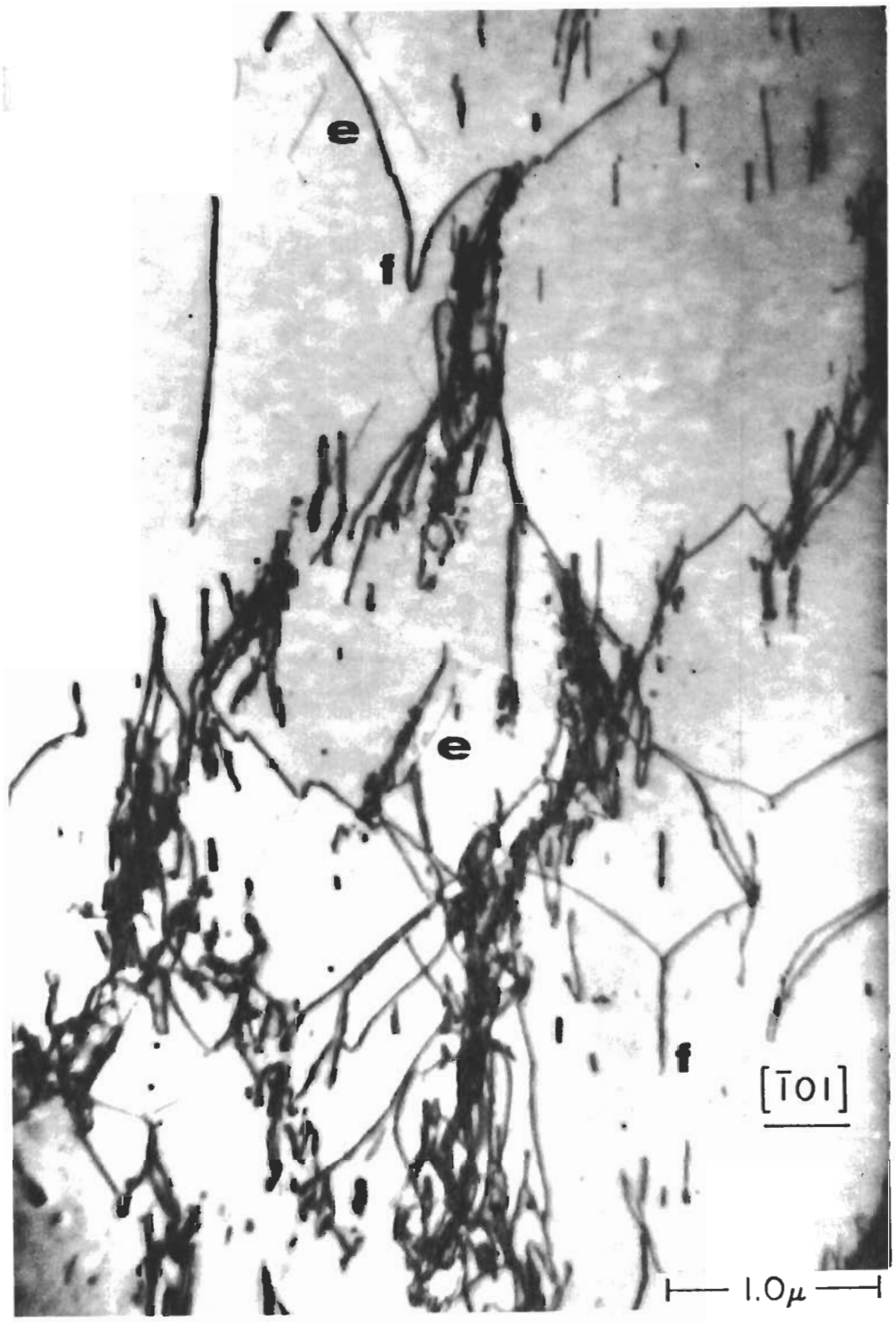

(C)

Figure 21 (Concluded)

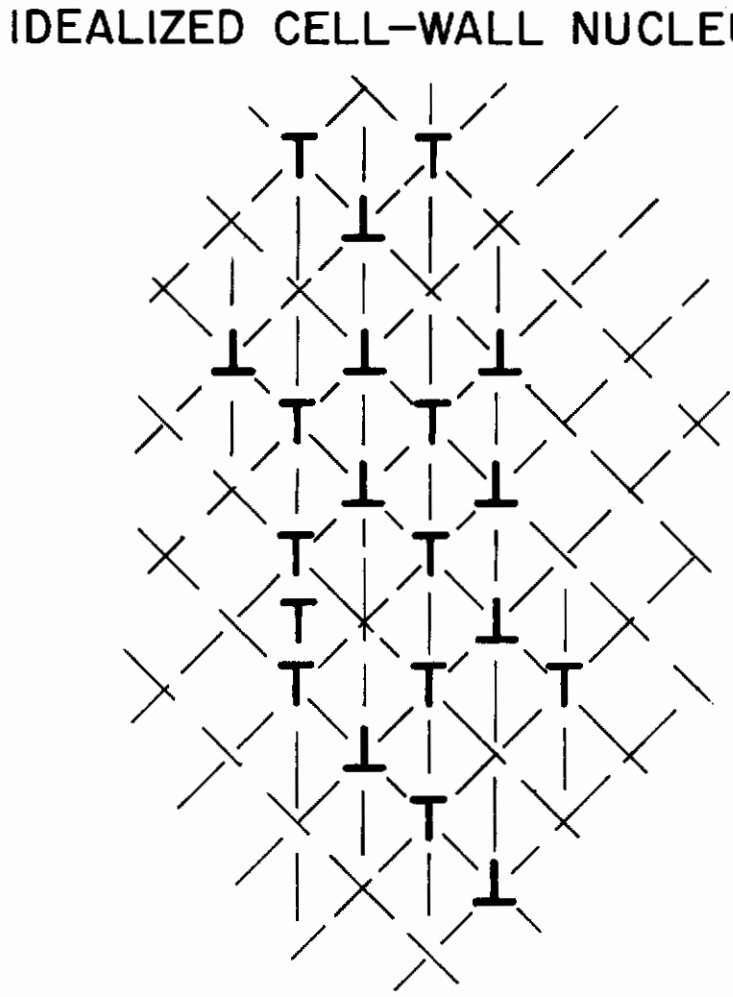

Figure 22 - Schematic Illustration of the Low-Energy Cell-Wall Configuration During the Earliest Stages of Rapid Hardening

Unclassified
Security Classification

DOCUMENT CONTROL DATA - R & D

(Security classification of title, body of abstract and indexing annotation must be entered when the overall report is classified)

1. ORIGINATING ACTIVITY *(Corporate author)* Midwest Research Institute 425 Volker Boulevard Kansas City, Missouri 64110	2a. REPORT SECURITY CLASSIFICATION Unclassified 2b. GROUP

3. REPORT TITLE

MECHANISMS OF FATIGUE HARDENING IN COPPER SINGLE CRYSTALS

4. DESCRIPTIVE NOTES *(Type of report and inclusive dates)*

Technical Report (1 April 1966 - 31 March 1967)

5. AUTHOR(S) *(First name, middle initial, last name)*

J. R. Hancock
J. C. Grosskreutz

6. REPORT DATE July 1967	7a. TOTAL NO. OF PAGES 48	7b. NO. OF REFS 23
8a. CONTRACT OR GRANT NO. AF 33(615)-3987 b. PROJECT NO. 7353 c. Task No. 735301 d.	9a. ORIGINATOR'S REPORT NUMBER(S) AFML-TR-67-203 9b. OTHER REPORT NO(S) *(Any other numbers that may be assigned this report)*	

10. DISTRIBUTION STATEMENT This Document is subject to special export controls and each transmittal to foreign governments or foreign nationals may be made only with prior approval of the Metals and Ceramics Division (MAM), Air Force Materials Laboratory, Wright-Patterson AFB, Ohio 45433

11. SUPPLEMENTARY NOTES	12. SPONSORING MILITARY ACTIVITY Air Force Materials Laboratory (RTD) Air Force Systems Command Wright-Patterson AFB, Ohio 45433

13. ABSTRACT An investigation of fatigue-hardening mechanisms in copper single crystals oriented for single slip was carried out for fully-reversed push-pull tests at a total resolved shear-strain amplitude of ± 0.008. Hysteresis loops and fatigue-hardening curves were recorded, and the dislocation structures were studied in annealed specimens and in cyclically hardened specimens after 4-1/2, 20, 100, and 660 cycles. Control specimens were irradiated with fast neutrons to prevent the loss and/or rearrangement of dislocations during electrothinning for transmission electron microscopy. No significant differences in dislocation density or morphology were detected between the irradiated and unirradiated crystals.

Fatigue hardening occurred by the accumulation and storage of dislocations into low-energy configurations characteristic of Stage I tensile hardening. The rapid-hardening stage was characterized by the rapid multiplication of dislocations and the build-up of cell-wall nuclei by the mutual trapping of primary edge dislocations on parallel slip planes. As cyclic straining proceeded, dislocations in the cell-wall nuclei became more densely packed and fragmented, and linked up to form a cell structure as saturation hardening developed. During saturation hardening, the applied strain could be accommodated by the traffic of dislocations across cells and/or cell-wall motion.

This abstract is subject to special export controls and each transmittal to foreign governments or foreign nationals may be made only with prior approval of the Metals and Ceramics Division(MAM), Air Force Materials Laboratory, Wright-Patterson AFB, Ohio 45433.

DD FORM 1 NOV 65 1473

Unclassified
Security Classification

14. KEY WORDS	LINK A		LINK B		LINK C	
	ROLE	WT	ROLE	WT	ROLE	WT
Fatigue Hardening						
Copper Single Crystals						
Dislocation Arrangements						
Transmission Electron Microscopy						
Dislocation Loss in Thin Foils						